Comparison of burning velocity differences in a numerical explosion simulator

Knut-Arne Vik

A thesis submitted in partial fulfilment of the
requirements for the degree of *Master of Science* in
the subject of Process Safety Technology

Department of Physics and Technology
University of Bergen
Bergen, Norway
June 2, 2014

Abstract

A verification study of the two flame models in the numerical explosion simulation tool FLACS has been conducted. The β flame model, and the SIF flame model has been tested in a 1D-channel at different time step sizes. Methods for measuring the flame speed has been discussed, and a best practice method has been chosen. The 1D-channel has been tested for closed end ignition and open end ignition. The possible introduction of a Fourier number as a stability criteria is also discussed.

Acknowledgements

First of all I would like to than GexCon AS for allowing me to write my Master Thesis in collaboration with their R&D department. It has been an honour to work among the competent and friendly staff at the Bergen office.

I would also like to thank my two supervisors Bjørn J. Arntzen (UoB) and Bjørn Lilleberg (GexCon) for their continuing support, and motivation. The motivational "pep talks", and academic discussions have been much appreciated.

Next I would like to thank Helene H. Pedersen for the tremendous amount of help I have received. Everything from start up help, to proofreading of my manuscripts, and continuous motivation. I dare to say that this research would not have come together without your help.

I am also very grateful to my proofreading friends Lise Fimland, Morten N. Holme, and Håvard Sognnes. Thank you for taking the time to read trough my manuscript, and giving me feedback.

Last, but not least I would like to thank my loving wife Kristin for her continuing support and motivation through the year. Thank you for pushing me, and keeping up with me during the final weeks before deadline.

Contents

List of Figures

List of Tables

Nomenclature

Roman letters

A	Area	m^2
a	Speed of sound	ms^{-1}
c	Progress variable	-
c_q	Minimum c where $w > 0$	-
C	General constant	-
C_p	Specific heat capacity at constant pressure	$\mathrm{JK}^{-1}\mathrm{kg}^{-1}$
$C_{1\varepsilon}$	Constant in the $k-\varepsilon$ equation; typically $C_{1\varepsilon} = 1.44$	-
$C_{2\varepsilon}$	Constant in the $k-\varepsilon$ equation; typically $C_{2\varepsilon} = 1.92$	-
$C_{3\varepsilon}$	Constant in the $k-\varepsilon$ equation; typically $C_{3\varepsilon} = 0.8$	-
C_{EBU}	Eddy Break-Up constant	-
C_μ	Constant in the $k-\varepsilon$ equation; typically $C_\mu = 0.09$	-
$\mathcal{D}$	Diffusion coefficient	$\mathrm{m}^2\mathrm{s}^{-1}$
E	Expansion ratio	-
F	Force	N
g	Gravitational acceleration	ms^{-2}
h	Specific enthalpy	Jkg^{-1}
k	Kinetic turbulence energy	$\mathrm{m}^2\mathrm{s}^{-2}$
L_{eg}	Length of grid extension	m
l	Length	m
l_t	Turbulence length scale	m
M_w	Molecular weight	kgmol^{-1}
$\dot{m}$	Mass rate	kgs^{-1}
n	Number of grid cells	-
p	Absolute pressure	Pa
P_ε	Production of dissipation rate of kinetic turbulence energy	$\mathrm{kgm}^{-1}\mathrm{s}^{-4}$
P_k	Production of kinetic turbulence energy	$\mathrm{kgm}^{-1}\mathrm{s}^{-3}$
$\dot{Q}$	Heat rate	Js^{-1}
R	Universal gas constant = 8.314	$\mathrm{Jmol}^{-1}\mathrm{K}^{-1}$
R_{fuel}	Reaction rate for fuel (source term in fuel equation)	$\mathrm{kgm}^{-3}\mathrm{s}^{-1}$
r	Stoichiometric oxidant-fuel ratio on mass basis	-
S	Burning velocity	ms^{-1}
S_{f}	Flame speed	ms^{-1}
S_L	Laminar burning velocity	ms^{-1}
T	Absolute temperature	K
t	Time	s
t_{f}	Characteristic flame time	s
t_η	Characteristic Kolmogorov time	s

U	Flow velocity ahead of the flame	ms^{-1}
u_i	Mean velocity (ith component)	ms^{-1}
u'	Turbulence intensity	ms^{-1}
V	Volume	m^3
w	Fuel reaction rate	$\mathrm{kgm}^{-3}\mathrm{s}^{-1}$
W	Dimensionless reaction rate	-
x	Length coordinate	m
Y	Mass fraction	-

Greek letters

β_i	Area porosity in the i th direction	-
β_v	Volume porosity	-
γ	Isentropic expansion factor	-
Δ	Grid cell size	m
Δt	Time step size	s
Δx	Grid cell size in x-direction	m
δ	Flame thickness	m
δ_{ij}	Kronecker delta function, $\delta_{ij} = 1$ if $i = j$. $\delta_{ij} = 0$ if $i \neq j$.	-
ε	Dissipation of kinetic turbulence energy	$\mathrm{m}^2\mathrm{s}^{-3}$
η	Kolmogorov length scale	m
μ	Dynamic viscosity	$\mathrm{Pa} \cdot \mathrm{s}$
μ_t	Dynamic turbulence viscosity	$\mathrm{Pa} \cdot \mathrm{s}$
μ_{eff}	Effective viscosity, $\mu_{\mathrm{eff}} = \mu + \mu_t$	$\mathrm{Pa} \cdot \mathrm{s}$
ν	Kinematic viscosity	$\mathrm{m}^2\mathrm{s}^{-1}$
ξ	Mixture fraction	-
ρ	Density	kgm^{-3}
σ_ϕ	Prandtl-Schmidt number.	-
σ_{ij}	Total stress tensor.	Nm^{-2}
τ_{ij}	Viscous stress tensor	Nm^{-2}
ϕ	General variable	-
χ	Mole fraction	-

Subscripts

b	Burnt	-
i	Spatial index	-
j	Spatial index	-
o	Sub-grid objects	-
ox	Oxidiser	-
P	Product	-
R	Reactant	-
t	Turbulence	-
u	Unburnt	-
v	Volume	-
w	Wall	-

Dimensionless groups

Fo	Fourier number, $\mathrm{Fo} = \frac{\mathcal{D}t}{l^2}$	-
Ka	Karlovitz number, $\mathrm{Ka} = \frac{t_\mathrm{f}}{t_\eta}$	-
Le	Lewis number, $\mathrm{Le} = \frac{\mathrm{Sc}}{\mathrm{Pr}}$	-
Pr	Prandtl number, $\mathrm{Pr} = \frac{\nu}{\alpha} = \frac{\mu cp}{\lambda}$	-
Re	Reynolds number, $\mathrm{Re} = \frac{\text{inertial force}}{\text{viscous force}} = \frac{\rho l u}{\mu}$	-
Sc	Schmidt number, $\mathrm{Sc} = \frac{\nu}{D} = \frac{\mu}{\rho D}$	-

Abbreviations

CFD	Computational Fluid Dynamics	-
CFL	Courant-Friedrichs-Levy	-
CMR	Christian Michelsen Research	-
CV	Control Volume	-
DNS	Direct Numerical Simulation	-
EBU	Eddy-Break-Up Model	-
EDM	Eddy Dissipation Model	-
FLACS	FLame ACceleration Simulator	-
pdf	Probability Density Function	-
RANS	Reynolds Averaged Navier Stokes	-

FLACS variables

CFLC	CFL number based on speed of sound	-
CFLV	CFL number based on flow velocity	-
RFU	Combustion rate, R_fuel	$\mathrm{kgm^{-3}s^{-1}}$

Chapter 1

Introduction

In 2011, the world population reached 7 billion people. As the population grows and the economic situation is improved, the energy consumption increases. To face the challenges of fuelling the world with power, we have to look to alternative energy sources, but in the foreseeable future the world will still depend on conventional energy sources like oil and natural gas. As of 2011, over 55 % of the global energy consumption comes directly from oil and natural gas. If combustion related energy sources such as biofuel, waste and coal like substances are considered together with oil and natural gas, the share is almost 80 % (IEA, 2013). A lot of people are daily in presence of these energy sources. Consequently, it is imperative that the extraction and handling of flammable materials are done in a safe and responsible way.

Explosion and fire hazards are almost inevitable when dealing with combustible energy sources, and some of the most severe hazards in the energy industry are associated with the extraction of oil and natural gas. Leakage of combustible gas or vapour can lead to devastating outcomes if the conditions are right. A typical event tree for the release of a combustible gas/vapour is shown in Figure 1.1. The Piper Alpha accident (Cullen, 1990), where 167 persons lost their lives, is an example of the severe damage potential of accidental explosions. Great efforts have been made by the petroleum industry to prevent and mitigate the consequences of such events.

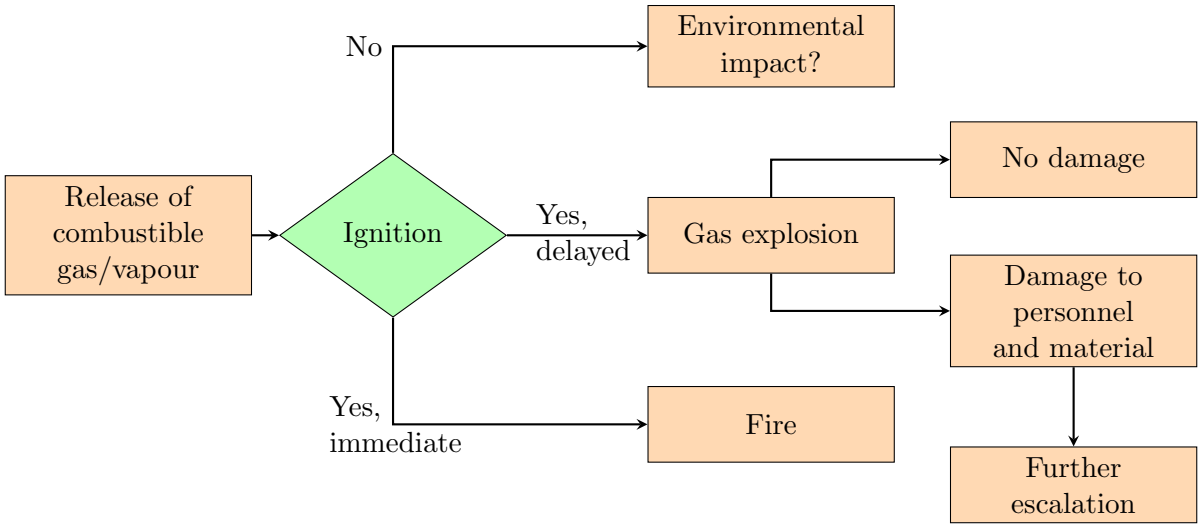

Figure 1.1: Simplified flowchart/event tree for the accidental release of combustible gas/vapour with focus on explosion, inspiration from Czujko (2001).

In order to design safe structures located in classified areas where explosions may occur, it is important to have knowledge of the potential explosion loads and forces acting on the structures during an explosion. Due to their high cost, large scale experiments are not ideal for evaluation of explosion loads in the concept phase of a new design. The information extracted from an experiment is also limited by the available sensors and measurement techniques. This have encouraged the development of computational codes which can simulate the physics of gas explosions. An overview of some of the different tools available for explosion consequence assessment is given by Park and Lee (2009).

The most sophisticated codes are within the field of computational fluid dynamics (CFD). CFD is a sub-field of fluid dynamics where the physical equations for fluid flow are solved numerically by means of a computer. Space is divided into boxes/cells termed control volumes (CVs), solutions for flow, thermodynamic properties etc. are calculated in each CV for different time steps. The CVs are linked together in a grid which compose the computational domain. Accordingly, a large spatial area defined by each control volume yields fewer control volumes in the computational domain, and consequently less computational time is needed for the simulation. Fluid flow at high velocities, and/or in congested geometries, are however often dominated by turbulence. To directly solve for flow with turbulence, the grid cell size needs to be smaller than the smallest motions, resulting in unfeasible long simulation times for large geometries like offshore platforms. Different sub-grid models are therefore used to model the activity within each cell, allowing for reasonable cell sizes.

For explosion modelling, there is also a need for a model to represent the flame. In the explosion simulator FLACS (flame acceleration simulator), the flame is modelled in two parts. The first part calculates a burning velocity based on different parameters such as; turbulence, gas mixture composition, and pressure. The second part takes the burning velocity, and models a flame that burns with the burning velocity. Changes have however been made to the code since the inclusion of this flame model. The numerical scheme used to solve the governing equations have among other things been changed. It therefore exists a need to verify how the flame model is performing under today's conditions. Verification is the process of checking that the different parts of the code performs the task they are supposed to. The gas explosion model evaluation protocol (MEGGE, 1996) also recommends that continuous verification should be performed on gas explosion tools like FLACS.

Chapter 2

FLACS

2.1 Background

The FLACS code is a numerical CFD tool specialising in modelling of gas explosion. Other capabilities, like dispersion studies, dust explosions, pool fires and jet fires are also available GexCon AS (2013). FLACS is developed and maintained by GexCon AS, a wholly owned subsidiary of Christian Michelsen Research (CMR). Development and validation of the code has been ongoing since the 1980s, with support from major oil and gas companies.

2.2 Governing equations for fluid flow

In this chapter, the governing equations for fluid flow used in FLACS are presented in Einstein notation (GexCon AS, 2013, pp. 325-326).

The following equation represents the conservation of mass:

$$\frac{\partial}{\partial t}(\beta_v \rho) + \frac{\partial}{\partial x_j}(\beta_j \rho u_j) = \frac{\dot{m}}{V} \tag{2.1}$$

where β_v is the volume porosity, ρ the density, β_j the area porosity in j-direction, and u_j the mean velocity in j-direction. The source/sink term on the right hand side accounts for, e.g. introduction of mass due to a leak, where $\dot{m}$ is the mass rate and V the volume of the CV. The conservation of momentum can be written in the same manner:

$$\frac{\partial}{\partial t}(\beta_v \rho u_i) + \frac{\partial}{\partial x_j}(\beta_j \rho u_i u_j) = -\beta_v \frac{\partial p}{\partial x_i} + \frac{\partial}{\partial x_j}(\beta_j \sigma_{ij}) + F_{o,i} + \beta_v F_{w,i} + \beta_v(\rho - \rho_0) g_i \tag{2.2}$$

$$F_{o,i} = -\rho \left| \frac{\partial \beta}{\partial x_i} \right| u_i |u_i| \tag{2.3}$$

where p is the absolute pressure, σ_{ij} the total stress tensor given by Equation 2.12. $F_{o,i}$ and $F_{w,i}$ are resistance to flow due to sub-grid obstructions and walls respectively, and g_i is the gravitational force. $F_{o,i}$ is given by Equation 2.3, and the derivative representing change in porosity is included to account for objects extending through several grid cells. If the derivative is zero, no extra form drag is included.

The equation of state used in FLACS is the ideal gas law:

$$pM_w = \rho RT \tag{2.4}$$

where M_w is the molecular weight of the gas mixture, R is the universal gas constant, and T the temperature. The enthalpy in FLACS, h, is calculated from a second order polynomial of the temperature (Arntzen, 1998, pp. 20-23):

$$h = h^0 + \int_{T_0}^{T} C_p dT = aT + \frac{1}{2}bT^2 - d \tag{2.5}$$

where h^0 is the standard heat of formation, C_p the specific heat, and a, b and d are component specific coefficients.

Turbulence is of considerable interest in many engineering applications, from flow around vehicles, to fluid processing and combustion. Turbulence occurs when the instabilities of a flow can no longer be damped by the viscosity of the fluid (Turns, 2012, p. 428). When the instabilities are too great, the result is the characteristic swirling motion that makes turbulence preferable in e.g. mixing processes. Figure 2.1 showcase some of the nature of a flow with turbulence. The transition to turbulence occurs when the Reynolds number (Re) reaches its critical value. Re is defined as:

$$\mathrm{Re} = \frac{\rho u l}{\mu} = \frac{u l}{\nu} \tag{2.6}$$

where l is a characteristic length of the system, e.g. the diameter for flow in a pipe, μ the

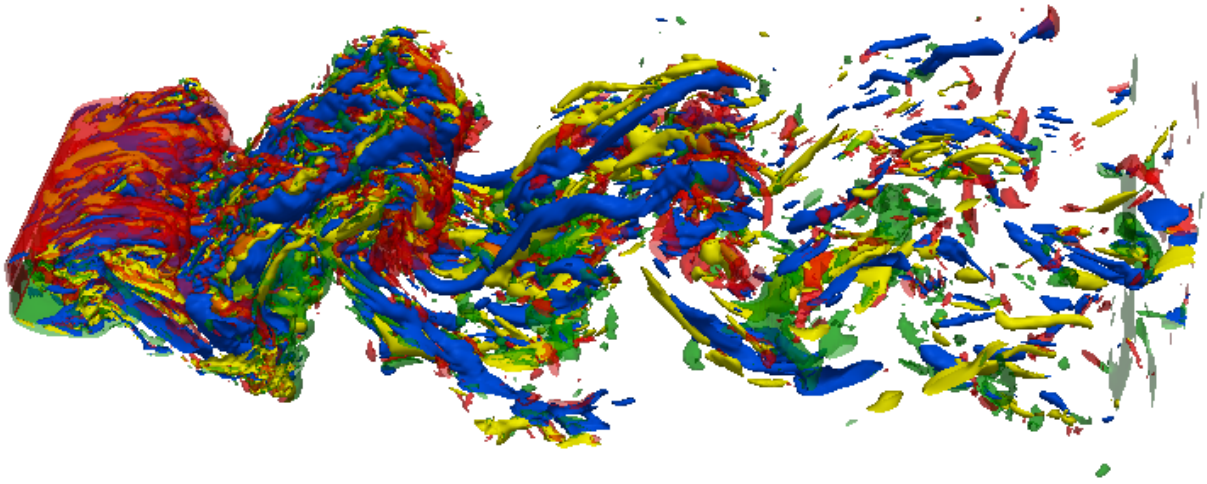

Figure 2.1: Direct numerical simulation of the turbulent wake behind a flat plate, from Narasimhamurthy (2009).

dynamic viscosity and ν the kinematic viscosity. As shown in Equation 2.6, Re is the ratio of the instability creating momentum, to the stabilising viscosity (Warnatz et al., 2006, p. 188). The transition from laminar to turbulent flow occurs at different conditions depending on the situation, e.g. for flow in a pipe, the transition is observed between Re = 2100 and Re = 4000 (McCabe et al., 2005, pp. 53-54). One notable feature of turbulence is the difference in size between the swirls. The swirls, often called eddies, can vary over several orders of magnitude (Wilcox, 1994, p. 4). As mentioned in Chapter 1, one of the challenges in CFD is the solution of turbulence. In theory it is possible to solve the Navier-Stokes equations with turbulence directly (Warnatz et al., 2006, pp. 189-190). This is known as direct numerical simulation (DNS) and

the numerical grid has to capture the movements of all the length scales involved. The problem with this is the large variation in the eddy length scales, resulting in a very high number of grid cells. The increased simulation time needed when dealing with reactive turbulent flow is addressed by Ertesvåg (2000, pp. 166-170). The smallest of the turbulence length scales l_t are called the Kolmogorov scales η. For some practical combustion problems (Ertesvåg, 2000), a length scale in the order of $\sim 10^{-4}$ is applied for η. For even a small scale industrial explosion, e.g. in a closed compartment of $2 \cdot 2 \cdot 3$ m, this η leads to a grid cell requirement of:

$$n = \frac{\text{Volume of computational interest}}{\text{Volume of the smallest grid cells}} = \frac{2 \cdot 2 \cdot 3}{(10^{-4})^3} = 1.2 \times 10^{13} \tag{2.7}$$

This assumes that the grid cell size is uniform in the whole computational domain. Even with less strict requirements, the time needed for DNS of reactive flow on a industrial scale, is far too long for all practical purposes. As a result DNS is still not available for engineering purposes on an industrial scale. To overcome the turbulence challenge a method called Reynolds averaging is applied.

Reynolds (1895) proposed to split the variables at hand into a mean value and a fluctuation. With a fluctuation as illustrated in Figure 2.2, the governing equation variables, ϕ, can be expressed as $\phi = \overline{\phi} + \phi'$. Averaging of each term results in what is known as Reynolds Averaged Navier Stokes (RANS). This method does however require the density to be regarded as constant,

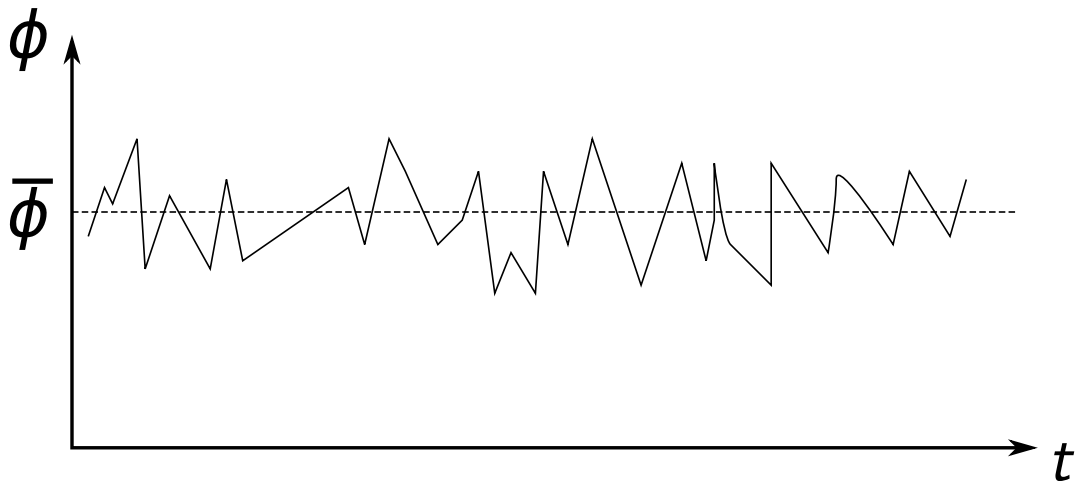

Figure 2.2: Fluctuation of variable ϕ around a mean value $\overline{\phi}$.

and since the density for most combustion purposes varies greatly, another averaging method called Favre averaging (Favre, 1965, 1969) is applied. The Favre averages are mass-weighted, and the difference from the Reynolds average is that the density is introduced in the average, as illustrated in Equation 2.8. Similarly, the variables are split into a mean, $\widetilde{\phi}$ and a fluctuation, ϕ''. In FLACS, the Favre averaging is used, and the transport equations (e.g. Equations 2.18 - 2.20) presented in this section are a result of this averaging.

$$\widetilde{\phi} = \frac{\overline{\rho\phi}}{\overline{\rho}} \tag{2.8}$$

Common for Reynolds and Favre averaging is that both methods introduce additional terms known as Reynolds stresses, $\widetilde{u_i'' u_j''}$ and turbulence fluxes, $\widetilde{u_j'' Y_{\text{fuel}}''}$, $\widetilde{u_j'' h''}$ and $\widetilde{u_j'' \xi''}$ (see e.g. Poinsot

and Veynante, 2005, pp. 140-143). Y_{fuel}, h and ξ are the fuel mass fraction, enthalpy and mixture fraction, respectively. The result of introducing these new terms is that the system of equations no longer is closed (there are more unknowns than equations), what is known as the closure problem of turbulence. In the following part are some of the models used to solve for the unknowns presented.

The Reynolds stresses and the viscous stresses are modelled in a similar manner by following the Boussinesq assumption. The viscous stress tensor τ_{ij} is defined as (Poinsot and Veynante, 2005, p. 7):

$$\tau_{ij} = \mu\left(\frac{\partial u_i}{\partial x_j} + \frac{\partial u_j}{\partial x_i}\right) - \frac{2}{3}\mu\frac{\partial u_k}{\partial x_k}\delta_{ij} \tag{2.9}$$

and the Reynolds stresses $\widetilde{\rho u_i'' u_j''}$ as (Poinsot and Veynante, 2005, p. 143):

$$-\widetilde{\rho u_i'' u_j''} = \mu_t\left(\frac{\partial u_i}{\partial x_j} + \frac{\partial u_j}{\partial x_i}\right) - \frac{2}{3}\delta_{ij}\left(\rho k + \mu_t\frac{\partial u_k}{\partial x_k}\right) \tag{2.10}$$

Equation 2.10 introduces the turbulence viscosity, μ_t, along with the kinetic turbulence energy, k, and the Kronecker delta function, δ_{ij}. The Kronecker delta is here defined as: $\delta_{ij} = 1$ if $i = j$ and $\delta_{ij} = 0$ if $i \neq j$. In contrast to the dynamic viscosity, the turbulence viscosity is not a thermodynamic property of the fluid, but a function of the flow (Ertesvåg, 2000, p. 39). The turbulence viscosity is combined with the dynamic viscosity to obtain the effective viscosity: $\mu_{\text{eff}} = \mu + \mu_t$. The turbulence viscosity is in the k-ε model (presented below) modelled as:

$$\mu_t = \rho C_\mu \frac{k^2}{\varepsilon} \tag{2.11}$$

By introducing μ_{eff}, equations 2.9 and 2.10 can be combined to yield an equation for the total stress tensor:

$$\sigma_{ij} = \tau_{ij} - \widetilde{\rho u_i'' u_j''} = \mu_{\text{eff}}\left(\frac{\partial u_i}{\partial x_j} + \frac{\partial u_j}{\partial x_i}\right) - \frac{2}{3}\delta_{ij}\left(\rho k + \mu_{\text{eff}}\frac{\partial u_k}{\partial x_k}\right) \tag{2.12}$$

The new unknowns are now k and μ_t. The turbulence model used most widely to handle this (Warnatz et al., 2006, p. 199), is the k-ε turbulence model presented in its standard form by Launder and Spalding (1974). The k-ε model solves two additional transport equations, one for the kinetic turbulence energy, k, and one for the dissipation of turbulence energy, ε. The transport equations for the kinetic turbulence energy and the dissipation rate of kinetic turbulence energy are respectively:

$$\frac{\partial}{\partial t}(\beta_v \rho k) + \frac{\partial}{\partial x_j}(\beta_j \rho u_j k) = \frac{\partial}{\partial x_j}\left(\beta_j \frac{\mu_{\text{eff}}}{\sigma_k}\frac{\partial k}{\partial x_j}\right) + \beta_v P_k - \beta_v \rho\varepsilon \tag{2.13}$$

$$\frac{\partial}{\partial t}(\beta_v \rho \varepsilon) + \frac{\partial}{\partial x_j}(\beta_j \rho u_j \varepsilon) = \frac{\partial}{\partial x_j}\left(\beta_j \frac{\mu_{\text{eff}}}{\sigma_\varepsilon}\frac{\partial \varepsilon}{\partial x_j}\right) + \beta_v P_\varepsilon - C_{2\varepsilon}\beta_v \rho\frac{\varepsilon^2}{k} \tag{2.14}$$

P_k is the production of kinetic turbulence energy and is the sum of the following contributing factors: flow shear stress, G_s, wall shear stress, G_w, buoyancy, G_b, and sub-grid objects, G_o.

$$P_k = G_s + G_w + G_b + G_o \tag{2.15}$$

P_ε is the production of turbulence dissipation rate, and $C_{2\varepsilon}$ a model constant. The different P_k factors, P_ε and their corresponding expressions can be found in the FLACS user manual (GexCon AS, 2013, p. 326). Hand in hand with the k-ε model comes a set of constants, and

Table 2.1: Constants and Prandtl-Schmidt numbers used in FLACS (GexCon AS, 2013, p. 327)

C_μ	$C_{1\varepsilon}$	$C_{2\varepsilon}$	$C_{3\varepsilon}$	σ_h	σ_{fuel}	σ_ξ	σ_k	σ_ε	σ_b
0.09	1.44	1.92	0.8	0.7	0.7	0.7	1	1.3	0.9

turbulence Prandtl-Schmidt numbers σ_ϕ. These are the same constants as the ones provided by Launder and Spalding (1974), and a complete list of all the values used in FLACS is presented in Table 2.1.

The turbulence fluxes, e.g. $\widetilde{u_j'' Y_{\text{fuel}}''}$, are on their hand modelled with a gradient model (Poinsot and Veynante, 2005, p. 142):

$$-\rho \widetilde{u_j'' Y_{\text{fuel}}''} = \frac{\mu_t}{\sigma_{\text{fuel}}} \frac{\partial Y_{\text{fuel}}}{\partial x_j} \tag{2.16}$$

Combining the turbulence flux and the diffusion term from the fuel mass fraction equation yields:

$$\frac{\partial}{\partial x_j}\left(\rho \mathcal{D} \frac{\partial Y_{\text{fuel}}}{\partial x_j} - \rho \widetilde{u_j'' Y_{\text{fuel}}''}\right) = \frac{\partial}{\partial x_j}\left(\left(\frac{\mu}{\sigma_{\text{fuel}}} + \frac{\mu_t}{\sigma_{\text{fuel}}}\right)\frac{\partial Y_{\text{fuel}}}{\partial x_j}\right) = \frac{\partial}{\partial x_j}\left(\frac{\mu_{\text{eff}}}{\sigma_{\text{fuel}}}\frac{\partial Y_{\text{fuel}}}{\partial x_j}\right) \tag{2.17}$$

$\mathcal{D}$ is the diffusion coefficient, linked to the Prandtl-Schmidt number as: $\sigma_{\text{fuel}} = \mu/(\rho\mathcal{D})$. Following this method, the transport equation for enthalpy h, fuel mass fraction Y_{fuel} and mixture fraction ξ is, respectively:

$$\frac{\partial}{\partial t}(\beta_v \rho h) + \frac{\partial}{\partial x_j}(\beta_j \rho u_j h) = \frac{\partial}{\partial x_j}\left(\beta_j \frac{\mu_{\text{eff}}}{\sigma_h}\frac{\partial h}{\partial x_j}\right) + \beta_v \frac{Dp}{Dt} + \frac{\dot{Q}}{V} \tag{2.18}$$

$$\frac{\partial}{\partial t}(\beta_v \rho Y_{\text{fuel}}) + \frac{\partial}{\partial x_j}(\beta_j \rho u_j Y_{\text{fuel}}) = \frac{\partial}{\partial x_j}\left(\beta_j \frac{\mu_{\text{eff}}}{\sigma_{\text{fuel}}}\frac{\partial Y_{\text{fuel}}}{\partial x_j}\right) + R_{\text{fuel}} \tag{2.19}$$

$$\frac{\partial}{\partial t}(\beta_v \rho \xi) + \frac{\partial}{\partial x_j}(\beta_j \rho u_j \xi) = \frac{\partial}{\partial x_j}\left(\beta_j \frac{\mu_{\text{eff}}}{\sigma_\xi}\frac{\partial \xi}{\partial x_j}\right) \tag{2.20}$$

The σ in Equation 2.18, 2.19 and 2.20 are turbulence Prandtl-Schmidt numbers, μ_{eff} is the effective viscosity, R_{fuel} is the fuel reaction rate handled by the combustion model (see Section 2.3), and $\dot{Q}$ is the rate of heat added to the system. The notation Prandtl-Schmidt is here used for both Prandtl (Pr) and Schmidt (Sc) numbers. This simplification is done because their use and significance are similar, and the Lewis number, $Le = Sc/Pr$ is assumed to be 1 (Warnatz et al., 2006, p. 120). This assumption signifies that the thermal diffusivity and mass diffusivity are regarded as equal. The Prandtl number is the ratio between the momentum diffusivity and the thermal diffusivity, while the Schmidt number is the ratio between the momentum diffusivity and the mass diffusivity (Ertesvåg, 2000, p. 241).

2.3 Combustion modelling

Combustion is typically separated into the distinct conditions non-premixed and premixed. In non-premixed combustion, the fuel and the oxidiser are mixed during the combustion process, while in premixed combustion, the fuel and oxidiser are already mixed before ignition. The theory presented here is for premixed combustion, as gas explosions only occur under premixed conditions (Eckhoff, 2005, p. 11).

If a premixed cloud with the right fuel/air ratio is ignited, the flame will travel from the ignition point, through the cloud. In order to initiate combustion, the reactants need to be heated. The heating process of the reactants is controlled by heat transfer from the hot products into the reactants. The speed at which this occurs, and hence the flame speed, increases greatly with the amount of turbulence, due to the improved mixing at the flame front. With no interference, the flame in a quiescent homogeneous fuel/air mixture, will travel at its lowest speed, the laminar burning velocity S_L. Some maximum values for S_L are presented in (Eckhoff, 2005, p. 15). The different regimes encountered in turbulent combustion can be illustrated in a Borghi diagram as in Figure 2.3. Re_t is the turbulence Reynolds number, and Ka the Karlovitz number defined

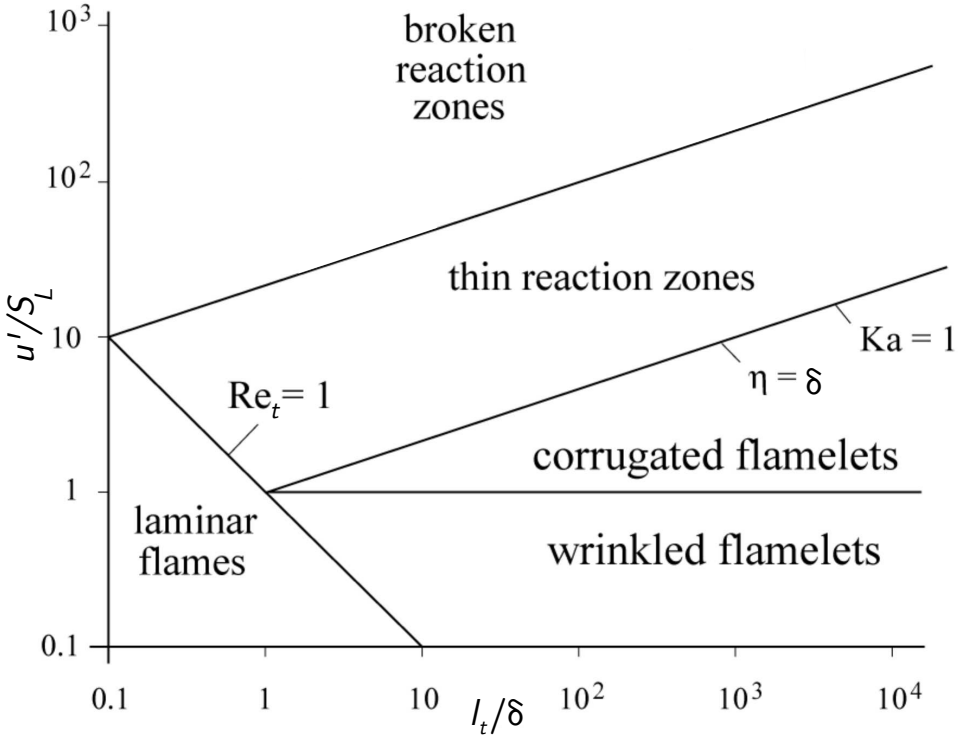

Figure 2.3: Borghi/regime diagram illustrating the different regimes in turbulent premixed combustion, based on Peters (2013); Borghi (1985).

as, respectively (Peters, 2000, p. 78):

$$\mathrm{Re}_t = \frac{u' l_t}{S_L \delta} \tag{2.21}$$

$$\mathrm{Ka} = \frac{t_\mathrm{f}}{t_\eta} = \frac{\delta^2}{\eta^2} \tag{2.22}$$

where u' is the turbulence intensity, l_t the turbulence length scale and δ the thickness of the flame. The Karlovitz number is the ratio of the characteristic flame time t_f to the characteristic time of the Kolmogorov eddies t_η. Outside of the laminar area with $\mathrm{Re}_t \leq 1$, the flames are turbulent to different extents. In the wrinkled flamelets area, turbulence intensity is less than or equal to the laminar burning velocity. The effect of this is that not even the largest eddies are able to compete with S_L, and the laminar burning is more dominant than corrugation by

the eddies. In the corrugated flamelets area the turbulence intensity is greater than the S_L. This allows the eddies to interfere with the flame front. This regime is however limited to areas where $\delta < \eta$. Because the flame thickness is smaller than η, the flame is embedded in the Kolmogorov eddies. Since η is the smallest scale, the flame structure inside the eddies will not be perturbed. In the thin reaction zones area, the flame thickness is greater than the Kolmogorov scale, allowing the eddies to enter the flame's preheat zone (see Figure 2.4). The inner layer of the flame is however still thinner than η, preserving the thin reaction zone. (Peters, 2000, pp. 78-81). The broken reaction zones regime is characterised by turbulence strong enough to cause local extinction (Peters, 2013).

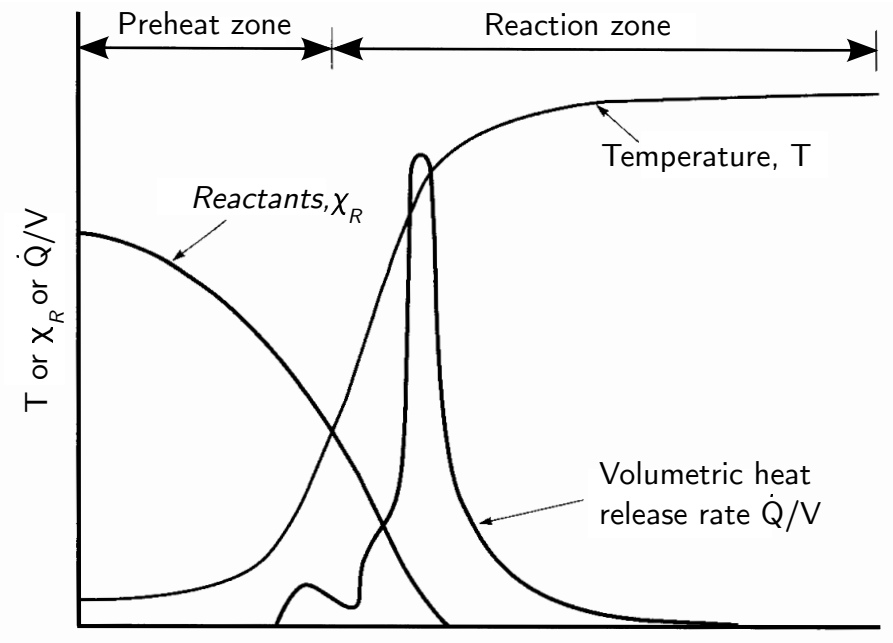

Figure 2.4: Structure of a laminar flame, based on a figure from (Turns, 2012, p. 260).

Reactive flow can be solved directly from basic principles like DNS for non reacting flow. This is however not possible for industrial scale applications, due to the tremendous amount of computational time needed. In the example by Ertesvåg (2000) mentioned in Section 2.2, the time needed for a simulation with combustion is estimated to $\sim 10^{16}$ times the time needed for an equivalent simulation without reaction. Flow with reaction is therefore in need of a model for the source term. The goal of the combustion models presented in this chapter is to close this source term.

The flamelet concept handles turbulent flames as an ensemble of smaller laminar flames embedded in a turbulence field. This concept is valid for all the areas where the flame thickness is smaller than Kolmogorov scale, and the flamelet concept is therefore useful in a wide range of combustion regimes. The chemistry can be regarded as fast, and the flame front to be thin (Peters, 2000, p. 50). From these assumptions, a progress variable c can be defined as:

$$c = \frac{T - T_u}{T_b - T_u} \qquad \text{or} \qquad c = \frac{Y_P}{Y_{P,b}} = 1 - \frac{Y_{\text{fuel}}}{Y_{\text{fuel},u}} \tag{2.23}$$

where T_u is the temperature in the unburnt gas, and T_b the temperature in the burnt gas. Y_P is the mass fraction of products, $Y_{P,b}$ the mass fraction of products in the burnt gasses, and $Y_{\text{fuel},u}$

the mass fraction of fuel in the unburnt gasses. The progress variable takes on values between 0 and 1 (0 in the unburnt gas and 1 in the burnt gas), and can therefore be used to locate the flame front. In the same manner as for the equations presented in Chapter 2.2, a transport equation can be written for the progress variable:

$$\frac{\partial}{\partial t}(\beta_v \rho c) + \frac{\partial}{\partial x_j}(\beta_j \rho u_j c) = \frac{\partial}{\partial x_j}\left(\beta_j \frac{\mu_{\text{eff}}}{\sigma_c}\frac{\partial c}{\partial x_j}\right) + w \tag{2.24}$$

where w is the reaction rate of fuel. Combining Equations 2.23 and 2.24, yields the mass fraction equation used in FLACS (Arntzen, 1998, p. 89):

$$\frac{\partial}{\partial t}(\beta_v \rho Y_{\text{fuel}}) + \frac{\partial}{\partial x_j}(\beta_j \rho u_j Y_{\text{fuel}}) = \frac{\partial}{\partial x_j}\left(\beta_j \frac{\mu_{\text{eff}}}{\sigma_{\text{fuel}}}\frac{\partial Y_{\text{fuel}}}{\partial x_j}\right) - Y_{\text{fuel},u} w \tag{2.25}$$

Spalding (1971) proposed to model the turbulent break up of lumps of unburnt gas as the rate determining action. This model is known as the eddy-break-up model (EBU), and uses the time scale of the turbulence as reaction time. The reaction rate for the reaction: 1 kg fuel + r kg oxidiser $\rightarrow (1 + r)$ kg product, can be written as (Ertesvåg, 2000, p. 160):

$$w_p = -(1 + r) w_{\text{fuel}} = C_{\text{EBU}} \frac{\varepsilon}{k} \rho \sqrt{\overline{Y''^2_{\text{fuel}}}} \tag{2.26}$$

where w_p and w_{fuel} is the reaction rate of the products and the fuel respectively, C_{EBU} is the Eddy Break-Up constant, and $\overline{Y''^2_{\text{fuel}}}$ is the variance of fuel mass fraction. Magnussen and Hjertager (1977) proposed the Eddy dissipation model (EDM) by substituting $\overline{Y''^2_{\text{fuel}}}$ with the mean mass fraction of the limiting species as presented in Equation 2.27 (Ertesvåg, 2000, p. 160).

$$w_{\text{fuel}} = A \frac{\varepsilon}{k} \rho \min\left(Y_{\text{fuel}}, \frac{1}{r} Y_{\text{ox}}, B \frac{1}{1 + r} Y_P\right) \tag{2.27}$$

A and B are model constants, and Y_{ox} is the mean mass fraction of oxidiser. One of the challenges with the EBU/EDM is that the grid cell size needs to be smaller than the integral length scale to resolve the flame, thus making it computationally extensive for large geometries.

2.3.1 β flame model

The β model (Arntzen, 1998) is the flame model currently used in FLACS (GexCon AS, 2013, p. 330). One of the main features of the β model is that the flame front representation and the burning velocity are calculated separately. The burning velocity is calculated by a burning velocity model, and the β model uses this velocity as input. The grid requirement $\Delta x < l_t$ is avoided in the β model, and hence allowing for coarser grid that can be used for industrial applications. The elimination of the grid requirement is done through a β transformation by increasing the turbulent diffusion coefficient $\mathcal{D}_t$ near the flame by a factor Δ / l_t. Simultaneously, the dimensionless reaction rate W is reduced by the same factor. By increasing $\mathcal{D}$, the flame is made thicker, allowing larger grid cells. The reaction rate used in the β model is a result of an eigenvalue analysis of the burning velocity, and testing of different probability density functions (pdfs) through the flame (Arntzen, 1998, p. 99):

$$w_\beta = W \rho \min\left(\delta(c - c_q), c, 9 - 9c\right) \tag{2.28}$$

Two relations need to be fulfilled, one for c_q (the minimum value of c with $w > 0$), and one for W:

$$\tau c_q = 0.325 \tag{2.29}$$

$$W\mathcal{D} = 1.37S^2 \tag{2.30}$$

The values of W and $\mathcal{D}$ are adjusted in FLACS to yield a flame thickness of around 3 grid cells.

2.3.2 Simple interface flame model

The simple interface flame model (SIF) for 3D models was introduced by Arntzen (1998). The model was developed as an improved alternative to the β-model, reducing the thickness of the flame from several grid cells to an interface in one cell. This gives a more realistic flame thickness as the grid cell size in FLACS often are in the range 0.4 - 1.0 m (Arntzen, 1998, p. 107). SIF treats the flame as an interface with zero thickness that converts reactants to products at a rate determined from the burning velocity and area of the flame. The SIF algorithm handles the combustion with two steps. The first step is the combustion part, where reactants are converted to products, and the second part convects the products to other cells, controlled by the velocity field. The burning velocity S is calculated by the same burning velocity model as in the β model. The mass of products in a cell with volume V, is changed by:

$$V\rho(c_1 - c_0) = S\rho_R A\Delta t \tag{2.31}$$

A is the area of the flame in the cell, ρ_R the density in the reactants and Δt the time step size. c_0 and c_1 is the progress variable before and after a time step. The cell is checked for products by evaluating; $c_1 \geq 1$. If the statement is true, all the reactants have been converted to products, and the flame goes on to the surrounding grid cells if they contain reactants. The method used to calculate the flame area A is described in (Arntzen, 1998, pp. 110-114).

2.4 Boundary conditions

The numerical boundaries in FLACS are handled by different boundary conditions specified at each boundary. The ones applicable for this research are the Symmetry, Euler and Plane Wave boundary conditions. The "Symmetry" condition mirrors the flow, and prevents flow from crossing the boundary. Variables are assumed to have zero-gradients over the boundary, i.e. no driving force for transport. This allows the boundary to act as a wall, without introducing wall-functions. The "Euler" condition solves the inviscid flow equations for outflow at the boundary, assuming ambient pressure outside the boundary. The problem with setting the pressure constant is that pressure waves can be reflected from the boundary. The Plane Wave condition was designed to avoid this reflection by extrapolating the pressure outside of the boundary. Plane Wave can however not be used close to the flame (Skjold et al., 2013; GexCon AS, 2013).

Chapter 3

Numerical 1D testing

In this chapter the main part om the research conducted will be presented. As mentioned in Chapter 1, an important part of explosion code maintenance is verification of the different modules. The β model will as the standard flame model in FLACS be tested in a range of 1D-tests. The SIF model will also be tested for verification purposes. Measures will be made to look at the flame models as isolated as possible, as the verification process focuses on each component by itself.

The numerical setup consists of a 10.0 m long channel, with a 1.0 m^2 quadratic cross section. The channel is open in one end, and closed in the other end. No physical walls are used in the setup, and the channel is instead enclosed by the "Symmetry" boundary condition in FLACS (see Figure 3.1). In the open end, the "Euler" boundary condition is used. Another possibility is to use the "Plane Wave" boundary condition in the open end. This was not done because of the limitation imposed by the fact that the flame should not reach the boundary.

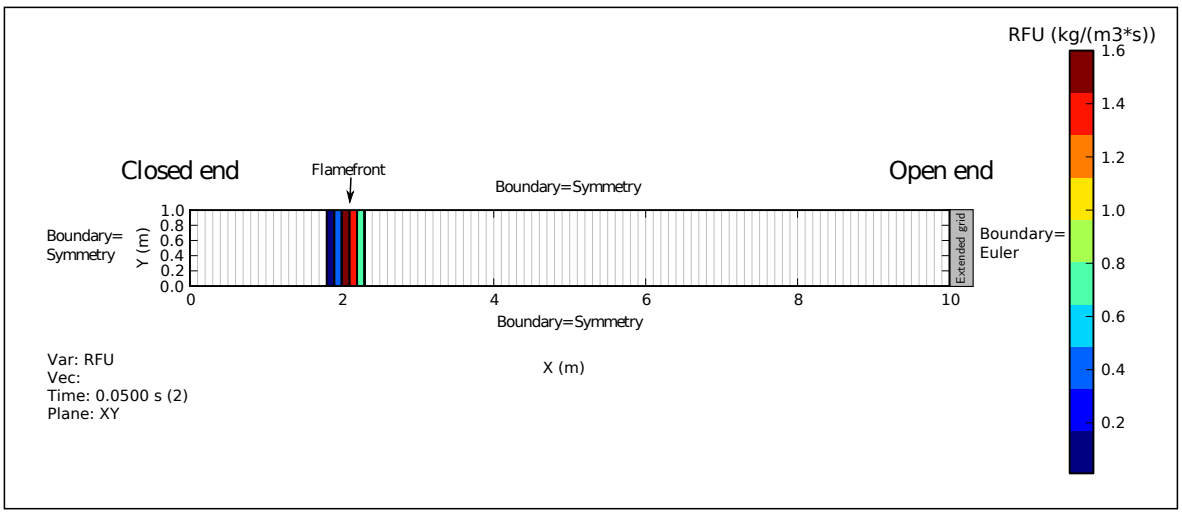

Figure 3.1: The 1D-tunnel during a closed end ignition with boundary conditions as described in the figure, and the grid stretched after 10 m (shown in figure 3.5). The variable RFU is the combustion rate in kg/(m^3s).

The reflection of pressure waves that "Plane Wave" eliminates is instead avoided by extension of the grid. The elimination of reflected pressure waves is more closely explained in Section 3.3.1.

Preliminary testing confirmed that "Euler" and "Plane Wave" as boundary condition in the open end gives the same results (see Figure 3.2). Furthermore, the grid resolution is constant at 1 grid cell in the yz-plane, and the number of grid cells is therefore only subject to variation in the x-direction.

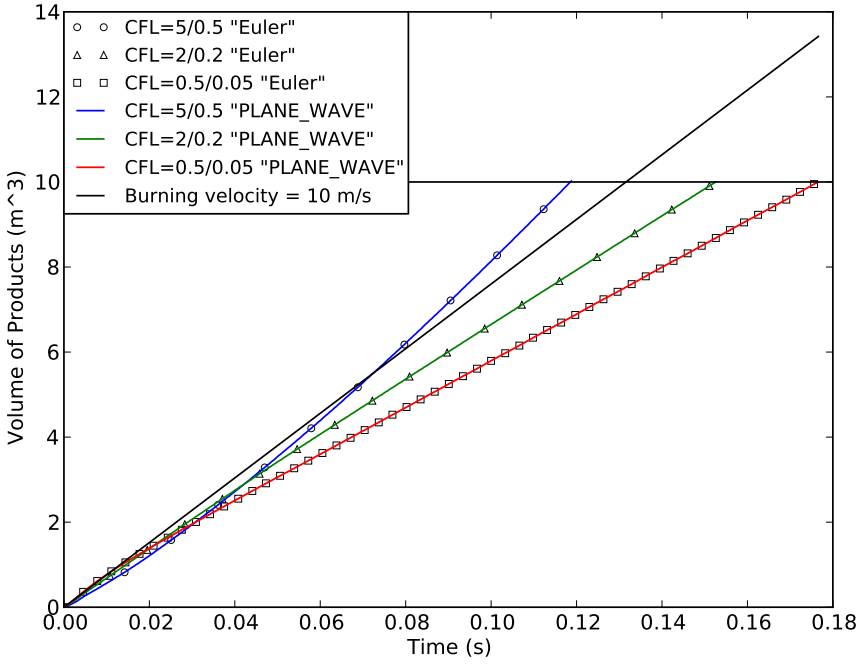

Figure 3.2: Result from the comparison of "PLANE WAVE" and "EULER" boundary conditions at the open end. The simulations are conducted with a burning velocity of 10 m/s, the grid cell size set to 0.1 m, and the time step sizes varied.

Ignition is initiated in either the open, or the closed end, and the flame propagates through the channel. This is illustrated in Figure 3.3.

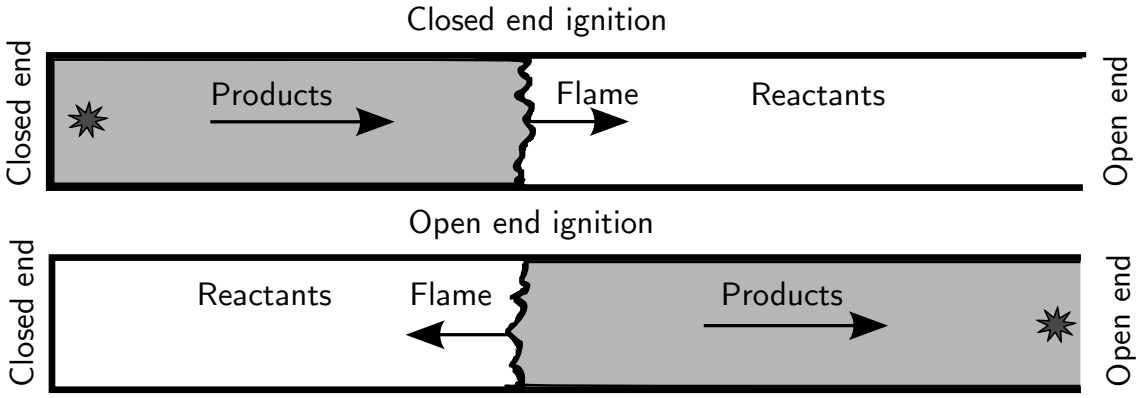

Figure 3.3: Illustration of the flow arrangement with closed and open end ignition.

When igniting in the open end of the channel, the flame will propagate inwards in the channel, while the combustion products will flow outwards. Ignition in the closed end will on the other hand cause both the flame and the combustion products to propagate/flow outwards. Because

the combustion products have nowhere to go, the flame front will be pushed forwards by the expanding hot products. This results in a much higher flame speed for outwards propagating flame than for inwards propagating. The hot products typically expand by a factor of 7-8 (Eckhoff, 2005, p. 21). The flame speed S_f is given as:

$$S_f = S + U = S \cdot E \tag{3.1}$$

where S is the burning velocity, U is the flow velocity ahead of the flame, and E is the expansion ratio.

As the governing equations are solved by numerical techniques that utilises loops through x, y and z directions, a few preliminary tests were run to discover possible differences with 1D flame propagation in the different spatial directions. The effect of gravity was disabled by setting the gravity constant in FLACS to zero.

Three identical cases (with the exception of channel direction), were created. The coordinate system for each test is presented in Figure 3.4a. The channel is 10 m in the direction written above the longest arrows. The different cases were tested at a burning velocity of 5 m/s with two different time step sizes. As seen in Figure 3.4b, the results were identical for the three cases, proving that 1D simulation in x-direction should be representative for all directions. Turbulence modelling was also disabled for the following simulations.

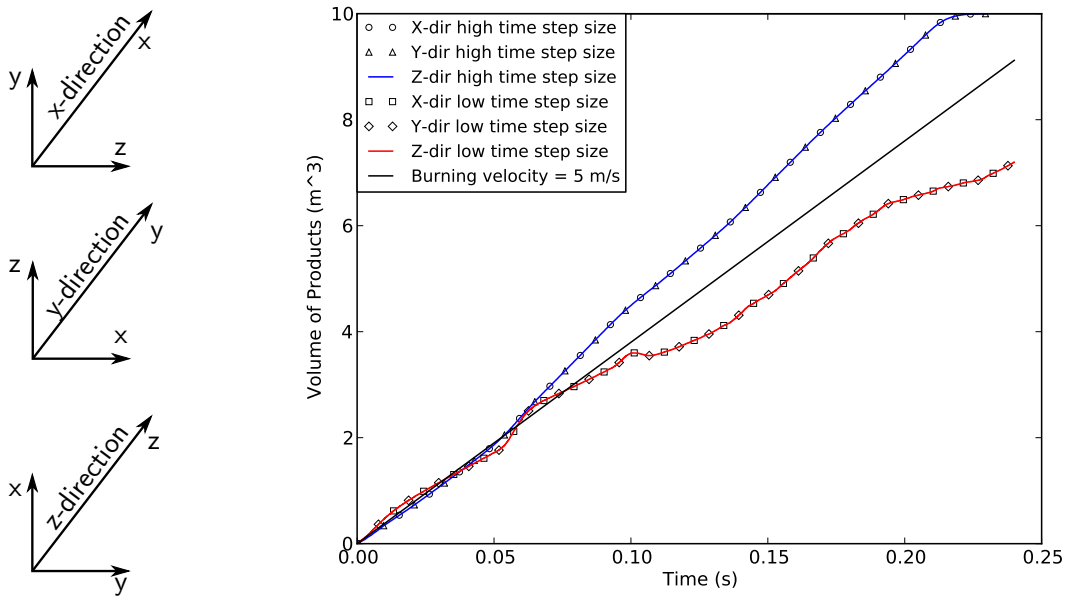

(a) The different channel directions.

(b) Test results for one large time step size, and for one small time step size.

Figure 3.4: 1D flame propagation in x-, y-, and z-direction.

3.1 Method for flame speed detection

There are several different approaches to to measure the flame speed. One method is to place monitor points in each grid cell, and measure the temperature throughout the simulation. When the temperature in a grid cell reaches a certain value, the flame can be regarded as detected in

that grid cell. Detection times can then be plotted against position in the numerical channel. The second method is to look at the total volume of products in the numerical domain. The flame front converts all the reactants to products, and the volume behind the flame will therefore always consist of products. Since the cross section of the channel is 1 m^2, directly plotting volume of products against time yields a meter per second plot. The last method was chosen because of its ease of use. This method does however set some limitations for the numerical domain, e.g. the grid can not be extended outside of the open end for open end ignition. In that case, the product gases expand into the volume outside the channel, and result in an increase in volume of products larger than the flame speed.

3.2 Fourier number

For unsteady diffusion processes, the dimensionless Fourier number Fo can be defined as (Holman, 2010; McCabe et al., 2005):

$$\mathrm{Fo} = \frac{\mathcal{D}t}{l^2} \quad \text{or} \quad \mathrm{Fo} = \mathcal{D}\frac{\Delta t}{(\Delta x)^2} \tag{3.2}$$

where $\mathcal{D}$ is the diffusion, Δt is the time step size, and Δx is the grid cell size (in x-direction). It is believed that Fo can be used to define a criteria for the time step size, that will result in a stable solution. The diffusion in the β model is given as (Arntzen, 1998, p. 99):

$$\mathcal{D} = CS\Delta x \tag{3.3}$$

where C is a constant, and S is the burning velocity. On these grounds, Fo was calculated for a range of the simulations. SIF do not incorporate a diffusion in the same way as the β model, and a Fourier number for SIF is therefore not straightforward to define. Due to limited time, Fourier number calculations were therefore only conducted for the simulations with the β model.

3.3 Closed end ignition with the β model

3.3.1 Pressure reflection from open end

The first tests revealed that it was difficult to get a stable flame speed with the chosen setup. When the initial gas cloud covered the whole channel, the flame accelerated after approximately 0.05 s, resulting in a significant deviation from the expected flame speed. To overcome the deviation, the channel was extended beyond the initial gas cloud, with the intention of minimising the effect. As seen in Figure 3.7, the distance the flame travels before it starts to accelerate, increases with the amount of stretched grid. The objective is to have a stable flame that corresponds to the chosen burning velocity through the 10 m channel. For a grid extended to 50 m and above, no acceleration is observed through the channel. The grid has to be extended by a length L_{eg}, to allow the flame to propagate throughout the 10 m channel, before the pressure wave has time to travel to the numerical boundary, and return. This is illustrated in Figure 3.6.

With a flame speed S_{f}, the time needed for the flame to burn through the 10 m channel is:

$$t_{\mathrm{flame}} = \frac{10}{S_{\mathrm{f}}} \tag{3.4}$$

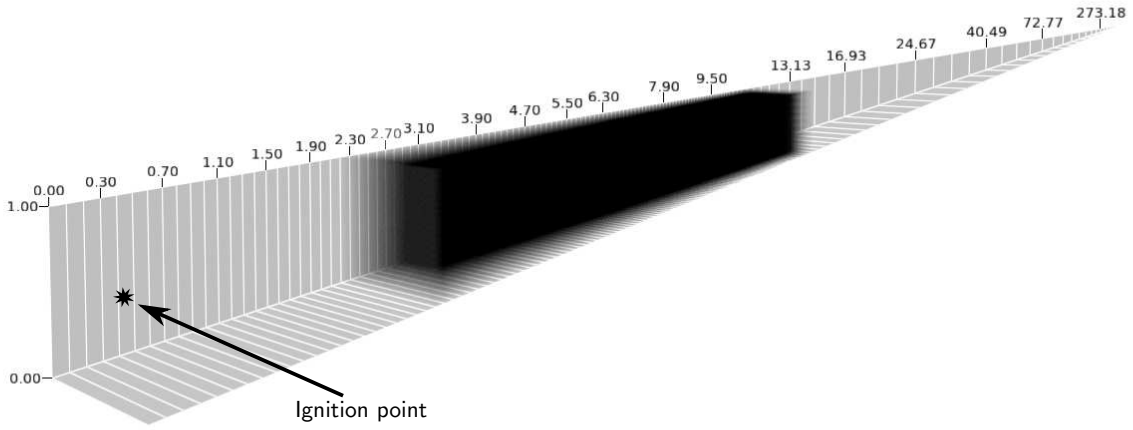

Figure 3.5: The same tunnel and ignition as figure 3.1 during a closed end ignition. The black area is unburnt gas. The grid is stretched after 10 m.

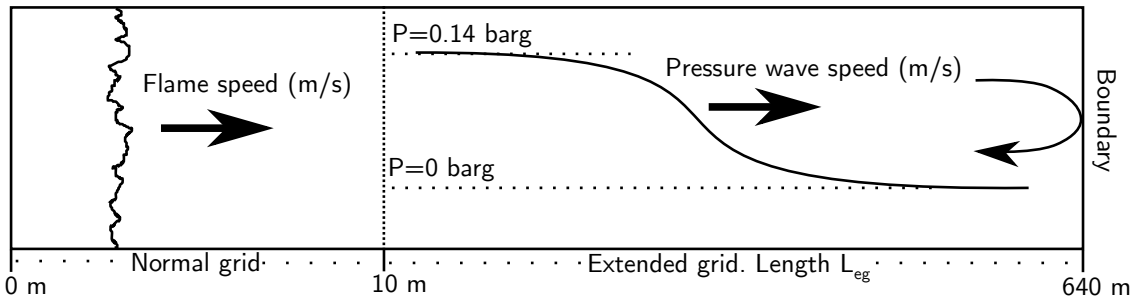

Figure 3.6: Illustration of the path the pressure wave has to travel to reach the flame front.

The time required for the pressure wave, travelling with sonic velocity, to return to the channel, depends on the length of the grid extension and is:

$$t_{\text{pressure}} = \frac{10 + 2L_{\text{eg}}}{a} \tag{3.5}$$

Combining equations 3.4 and 3.5 by setting $t_{\text{flame}} = t_{\text{pressure}}$, assuming that the speed of sound in the unburnt reactants is $a \approx 340$ m/s, and solving for L_{eg} yields:

$$L_{\text{eg}} = \frac{3400/S_{\text{f}} - 10}{2} \tag{3.6}$$

An example with burning velocity set to 5 m/s, and an expansion of 7.6 results in:

$$L_{\text{eg}} = \frac{3400/(5 \times 7.6) - 10}{2} \approx 39.7 \text{ m} \tag{3.7}$$

To circumvent a pressure wave from disturbing a flame front travelling at 38 m/s, it would be sufficient to extend the grid to above $10 + 39.7 \approx 50$ m. This is consistent with the observations in Figure 3.7.

From Figures 3.8 and 3.9, it is clear that for both extended and not extended grid, the pressure decreases after a given time. Compared to the non extended grid, this occurs at a later time for the extended grid. With decreasing burning velocity, the amount of extra grid necessary will increase. The grid is consequently extended to 640 m for the succeeding 1D-simulations. To avoid unnecessary long simulation times, and reduce storage space needed for the simulations, the extended grid is stretched in the x-direction (illustrated in Figure 3.10). The stretching results in a significant reduction in number of grid cells, e.g. for a grid cell size of 0.1 m, extended to 500 m, the number of grid cells is $n = 5000$. However, with a stretch factor of ~ 1.2, the number of grid cells is reduced to $n = 138$.

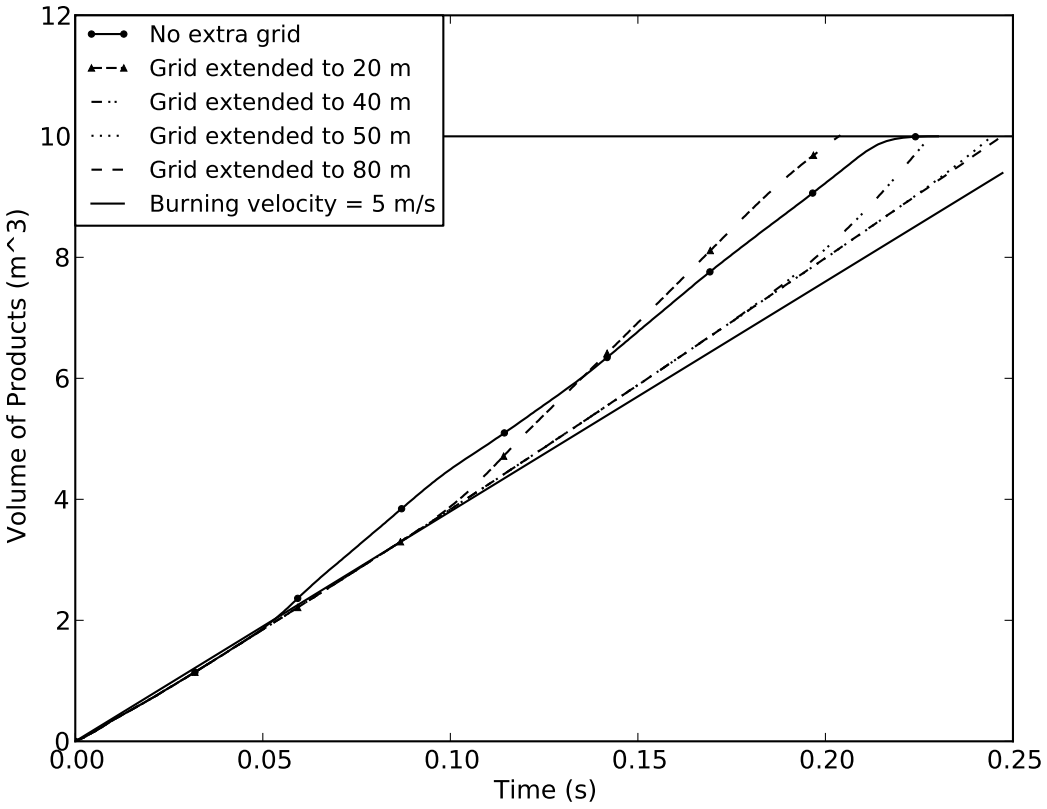

Figure 3.7: Simulations of closed end ignition with numerical grid stretched to different lengths. The burning velocity of 5 m/s gives together with the expansion ratio of 7.6 a flame velocity of 38 m/s. Following that the channel has a 1 m^2 cross section, the slope of the lines will have the unit of m/s.

3.3.2 Correction for long time steps

The β-model described in Section 2.3 includes a correcting function that impose a change in the reaction rate (RFU) for long time steps. Simulations have been run with and without this function, in an attempt to reveal effects masked by this function.

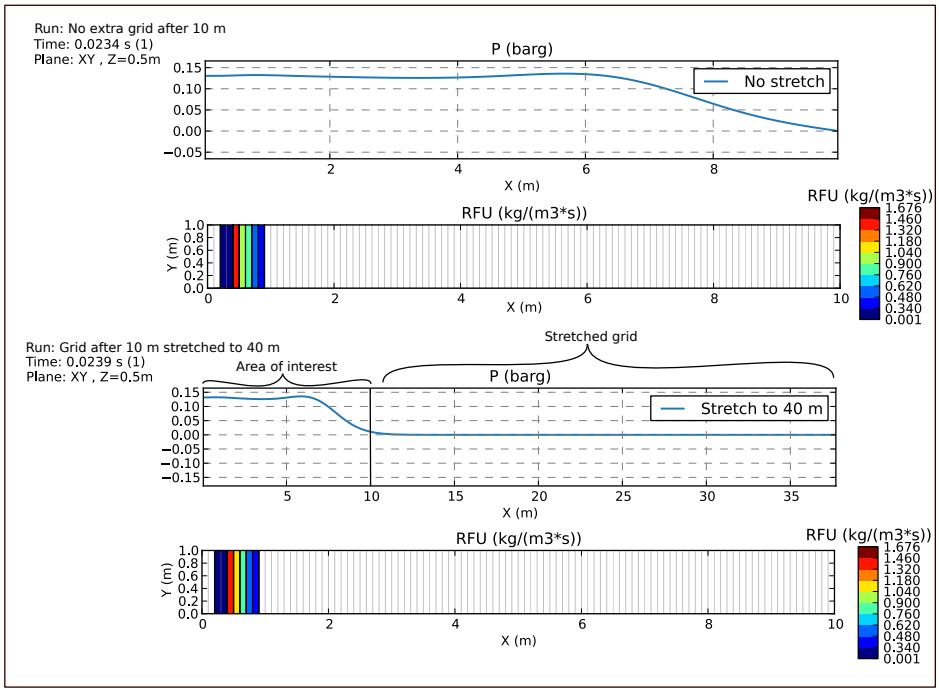

Figure 3.8: Effect of stretched grid after ~ 0.02 s. Upper two parts illustrate no extra grid, and bottom two illustrate stretch to 40 m.

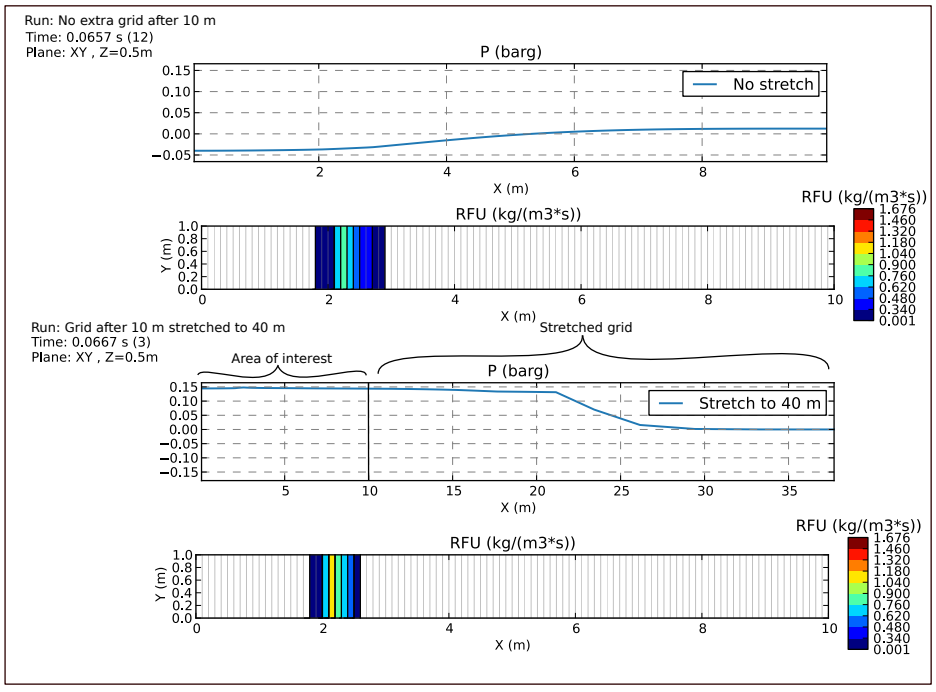

Figure 3.9: Effect of stretched grid after ~ 0.07 s. Upper two parts illustrate no extra grid, and bottom two illustrate stretch to 40 m.

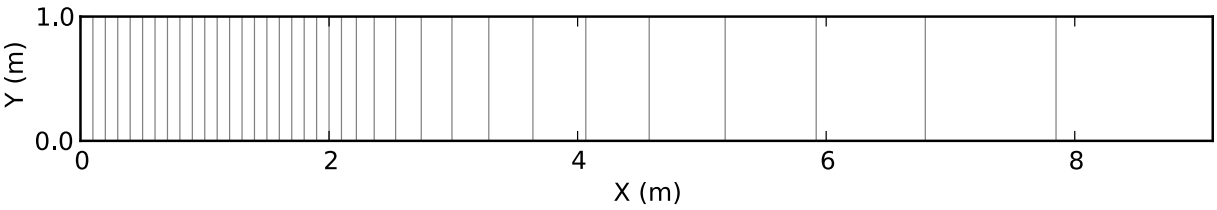

Figure 3.10: Example of a stretched grid. The grid cell size increases in the x-direction.

3.3.3 Time step testing

The 10 m channel was tested with different time step lengths to investigate the effect on the flame speed. FLACS uses two Courant-Friedrich-Levy (CFL) numbers to control the length of the time steps, namely CFLC and CFLV. CFLC is based on the sound velocity, and CFLV on the fluid flow velocity. The CFLC and CFLV numbers impose a time step limit for how long the sound waves, and the fluid flow can propagate, respectively, in a time step. The distance for both, is the average CV size multiplied by the CFL number. The time step size can be expressed as:

$$\Delta t = \min\left(\frac{CFLV\Delta x}{u}, \frac{CFLC\Delta x}{c}\right) \tag{3.8}$$

Following this criteria, the time step size will be limited by whichever is stricter. As an example, CFLC will be the limiting factor when flow velocities are low. The actual time steps utilised during the simulation were extracted post simulation. Normally the time steps will not vary significantly during the main part of flame propagation. However, when fluctuations in flame speed occurs, the time step size will also fluctuate. The time step size is therefore extracted as an average of the time steps throughout the run.

Testing was conducted systematically by first setting a burning velocity, and then running a number of simulations with decreasing CFLC/CFLV numbers. A set of typical CFL numbers applied in the simulations are presented in Table 3.1, some of the results with the correction factor are presented in Table 3.2, and some of the results without the correction factor are presented in Table 3.3. The factor of 10 between the CFLC and CFLV value is the standard used in FLACS.

Table 3.1: Typical CFLC and CFLV values used in the simulations

CFLC	5	3	2	1	0.5	0.05	0.01
CFLV	0.5	0.3	0.2	0.1	0.05	0.005	0.001

3.3.3.1 With correction

A number of different CFLC/CFLV numbers were tested with the burning velocity held constant at 0.67 m/s. The specific burning velocity was chosen to have a comparable set for open end ignition with $S_\mathrm{f} = 5$ m/s. Results from the simulation are shown in Figure 3.12. For all the time steps tested, the flame speed is approximately constant, but lower than the expected, and desirable value of ~ 5.09 m/s. Smaller time steps did not lead to notable change in S_f.

The burning velocity of 2.6 m/s was then tested for a range of different time steps. This burning velocity was also chosen with open end ignition in mind, this time with $S_\mathrm{f} \sim 20$ m/s. As seen from Figure 3.13, S_f converges towards a value below the theoretical value with decreasing time steps. Convergence is achieved with CFL values set to 3/0.3 and below.

Furthermore a series of different CFLC/CFLV numbers were tested with the burning velocity held constant at 5 m/s. The results of the simulations are shown in Figure 3.14. With the highest CFL values tested, 5/0.5, $S_f \sim 40.8$ m/s, i.e. somewhat high compared to the expected 38 m/s. On the other hand, the lower time steps results in flame speeds considerably lower (~ 28 m/s). As seen in Figure 3.14, the flame speed is converging for CFLC/CFLV values less than or equal to 2/0.2.

Increasing the burning velocity to 10 m/s, while lowering the time steps also resulted in similar deviations as for the lower velocities. As shown in Figure 3.15, the highest time step sizes results in accelerating, or slightly too high S_f, but for CFLC/CFLV numbers $\leq 1/0.1$, S_f converges towards ~ 55 m/s.

When further increasing the burning velocity to 20 m/s, the highest time steps resulted in accelerating S_f. Reducing the time steps further did not lead to convergence for S_f. With decreasing time steps, S_f first decreased, and then increased again. This is an interesting deviation from the convergence observed at lower burning velocities.

For all the tested burning velocities below 20 m/s, the flame speed converged towards a value ~ -26 % lower than the expected flame speed with an expansion of 7.6. The converged flame speeds are presented in Table 3.2. The Fourier numbers were also calculated for all the simulations, and plotted against the deviation from the correct flame speed in Figure 3.11. The results show that convergence is achieved at sufficiently low values of Fo. In this case values below 0.005 seems to be sufficiently small.

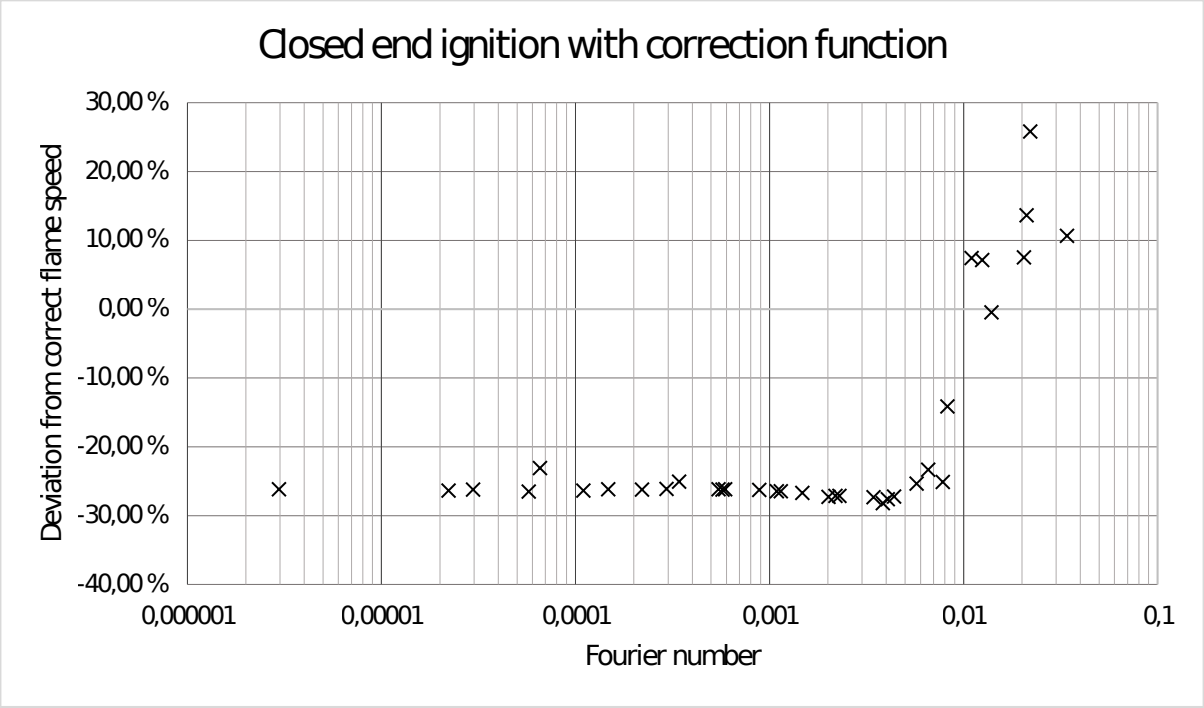

Figure 3.11: Deviation from the correct flame speed as a function of the Fourier number for closed end ignition with the β model, and the correction function enabled.

Table 3.2: Convergence results from closed end ignition with correction function

Velocity (m/s) Input	S_f with expansion	CFLC	CFLV	Converged S_f (m/s)	Percent deviation
0.67	5.092	0.01	0.001	3.759	-26.18
2.6	19.76	0.05	0.005	14.521	-26.51
5	38	0.05	0.005	27.981	-26.37
10	76	0.5	0.05	55.263	-27.29
20	152	0.01	0.001	116.926	-23.08

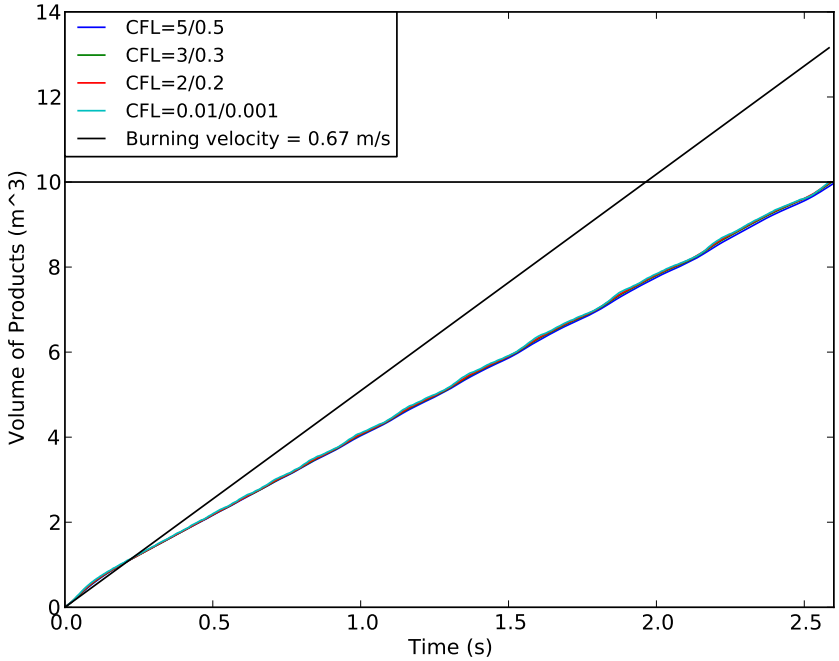

Figure 3.12: The result of variation of CFL values with the other parameters held constant, and with closed end ignition. The burning velocity is set to 0.67 m/s, and the grid cell size to 0.1 m. For decreasing CFL values, the flame speed is converging towards $\sim$ 3.76 m/s.

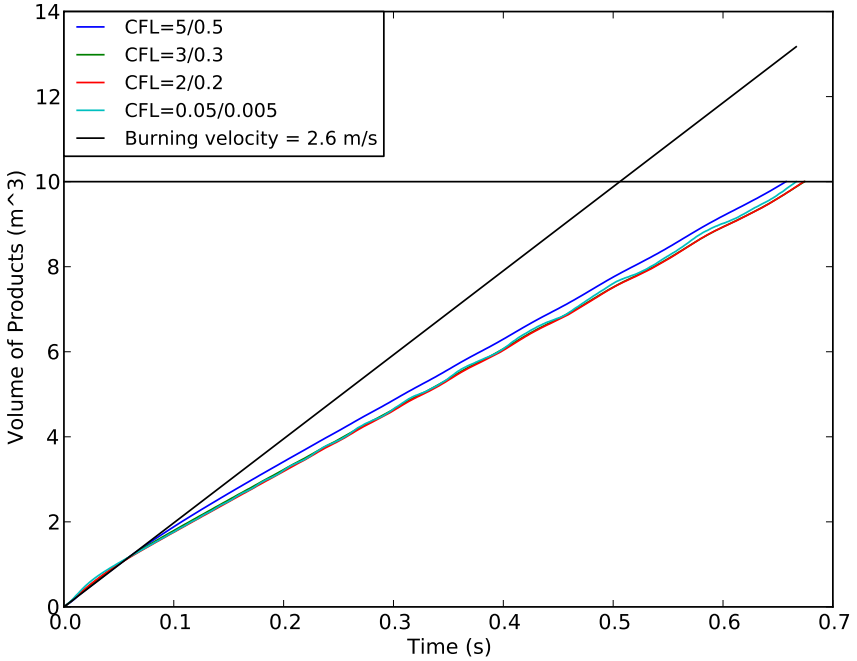

Figure 3.13: The result of variation of CFL values with the other parameters held constant, and with closed end ignition. The burning velocity is set to 2.6 m/s, and the grid cell size to 0.1 m. For decreasing CFL values, the flame speed is converging towards $\sim$ 14.5 m/s.

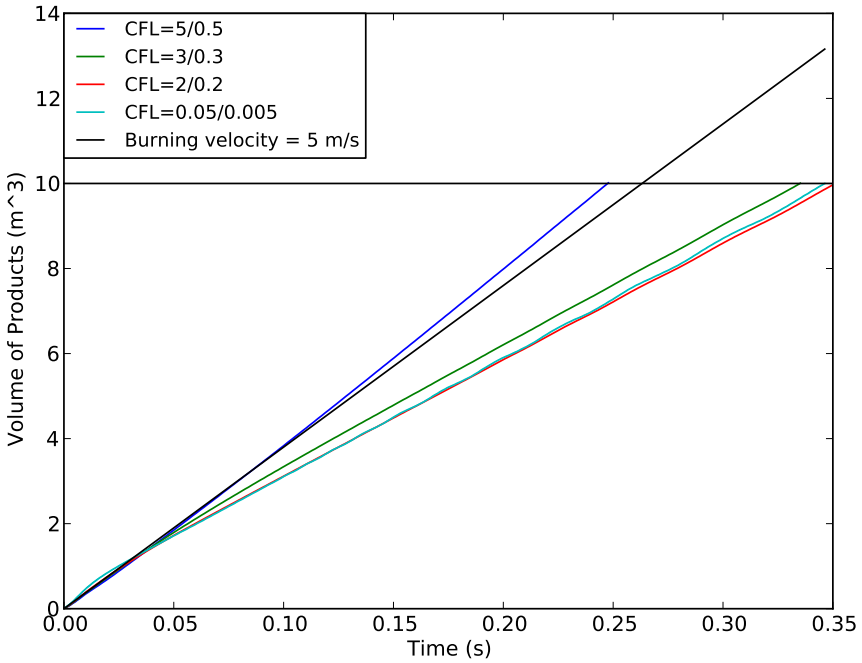

Figure 3.14: The result of variation of CFL values with the other parameters held constant, and with closed end ignition. The burning velocity is set to 5 m/s, and the grid cell size to 0.1 m. For decreasing CFL values, the flame speed is converging towards $\sim$ 28 m/s.

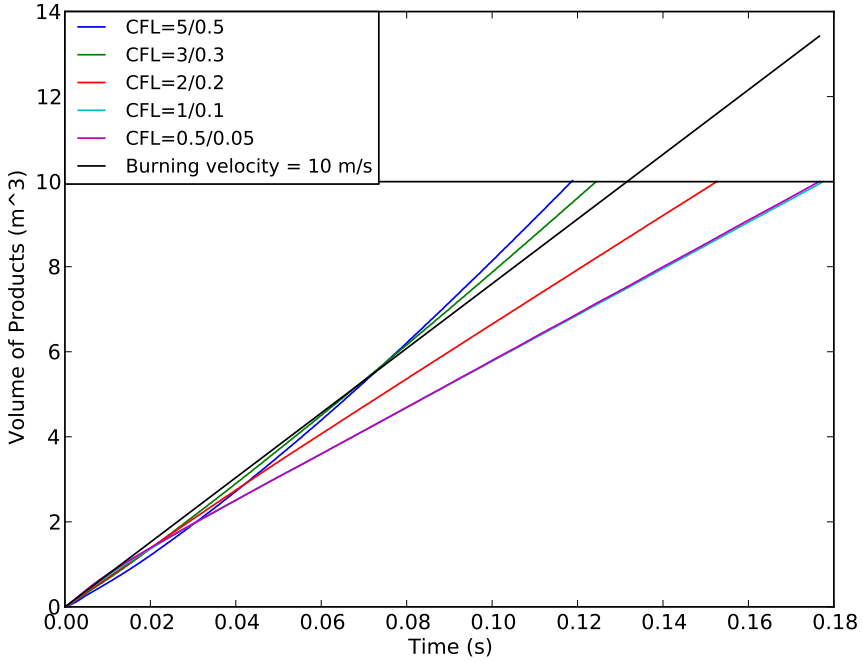

Figure 3.15: The result of variation of CFL values with the other parameters held constant, and with closed end ignition. The burning velocity is set to 10 m/s, and the grid cell size to 0.1 m. For decreasing CFL values, the flame speed is converging towards $\sim$ 55 m/s.

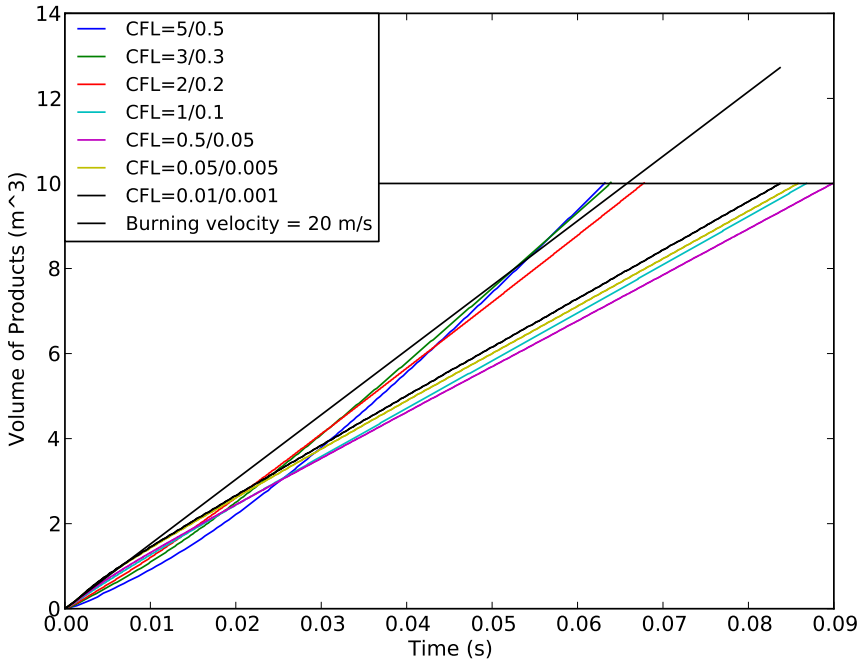

Figure 3.16: The result of variation of CFL values with the other parameters held constant, and with closed end ignition. The burning velocity is set to 20 m/s, and the grid cell size to 0.1 m. For decreasing CFL values, the flame speed first decreases, and then increases again.

3.3.3.2 Without correction

The same tests that were conducted with the inbuilt correction for long time steps, was also conducted without the correction. Accordingly, burning velocities of 0.67, 2.6, 5, 10 and 20 m/s were tested with lowering of the time step sizes.

The lowest burning velocity of 0.67 m/s resulted in a similar convergence as for the test with the correction function, but as seen in Figure 3.18; reducing of the time step size was necessary to get a converged flame speed. Increasing the burning velocity to 2.6 m/s, required even further reduction in time step size to reach convergence, as seen in Figure 3.19. With a burning velocity of 5 m/s, the same results were observed i.e. a convergence towards a too low flame speed, and as seen in Figure 3.20; strong acceleration at the highest time step size. Adjustment to 10 m/s did not result in full convergence within the range of time steps tested, but some degree was observed, as seen in Figure 3.21. Similar to the simulation with the correction function for 20 m/s, the simulation without it resulted in a flame speed lower than expected, but as seen in Figure 3.22; closer than for the burning velocities $\leq$ 10 m/s. If the results with and without the correction function is compared, the trend is the same; for burning velocities $\leq$ 10 m/s, the flame speed is converging towards a $S_\mathrm{f} \sim$ 26 % lower than the theoretical speed. For 20 m/s, the converging speed is closer to the theoretical value with a $S_\mathrm{f} \sim$ 23 % lower than expected. The Fourier numbers were also calculated for the simulations without the correction function, and the results are shown in Figure 3.17. Fourier numbers lower than ~ 0.003 were sufficient to reach convergence.

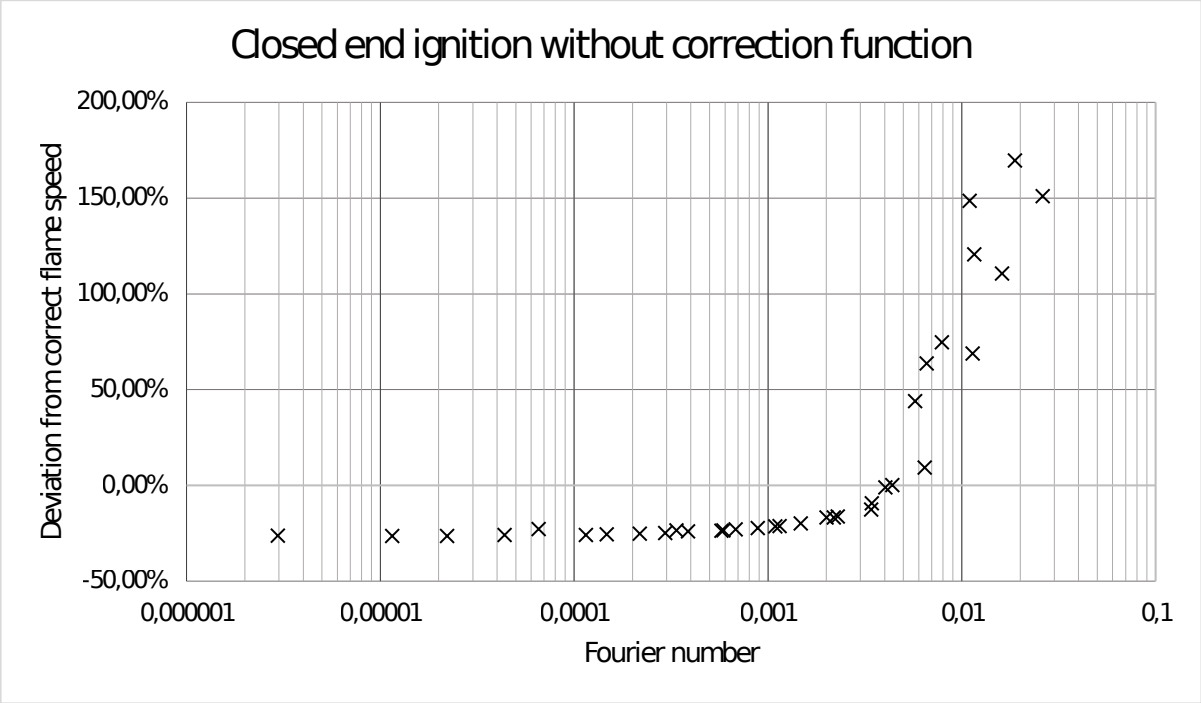

Figure 3.17: Deviation from the correct flame speed as a function of the Fourier number for closed end ignition with the β model, and the correction function disabled.

Table 3.3: Convergence results from closed end ignition without correction function

Velocity (m/s)					
Input	S_f with expansion	CFLC	CFLV	Converged S_f (m/s)	Percent deviation
0.67	5.092	0.01	0.001	3.76	-26.16
2.6	19.76	0.01	0.001	14.529	-26.47
5	38	0.01	0.001	27.992	-26.34
10	76	0.01	0.001	56.305	-25.91
20	152	0.01	0.001	117.456	-22.73

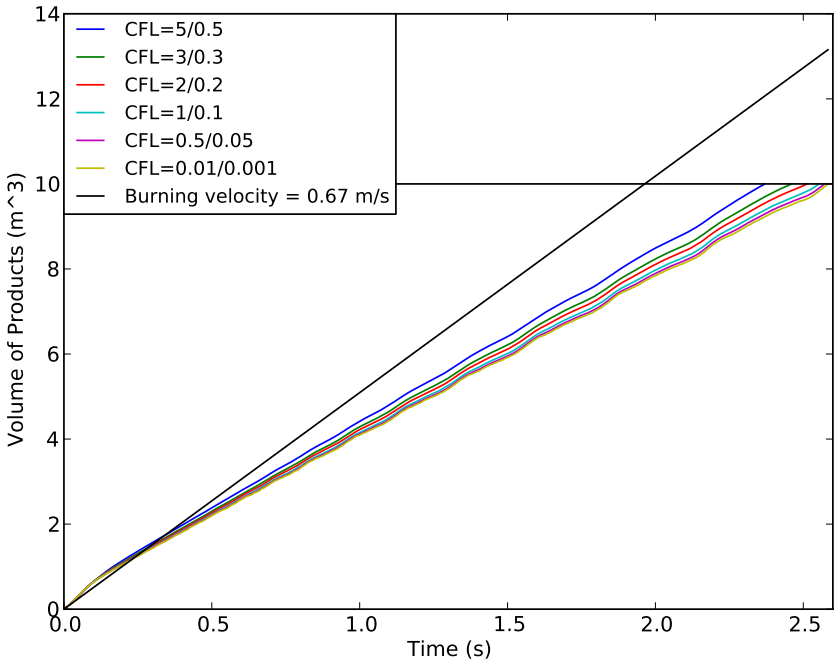

Figure 3.18: The result of variation of CFL values with the other parameters held constant, and with closed end ignition. The correction for long time steps is disabled, the burning velocity is set to 0.67 m/s and the grid cell size to 0.1 m. For decreasing CFL values, the flame speed is converging towards $\sim$ 3.76 m/s.

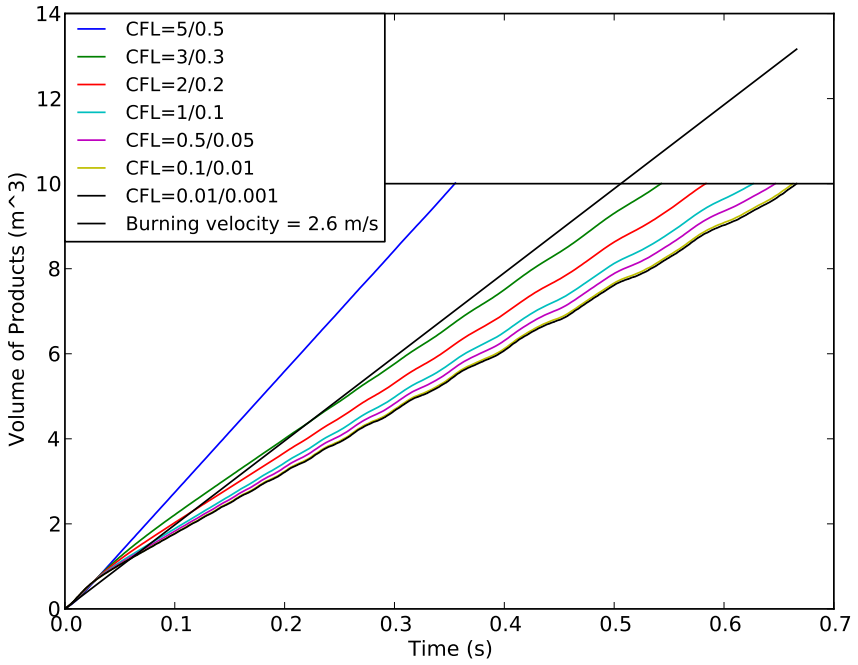

Figure 3.19: The result of variation of CFL values with the other parameters held constant, and with closed end ignition. The correction for long time steps is disabled, the burning velocity is set to 2.6 m/s and the grid cell size to 0.1 m. For decreasing CFL values, the flame speed is converging towards $\sim$ 14.5 m/s.

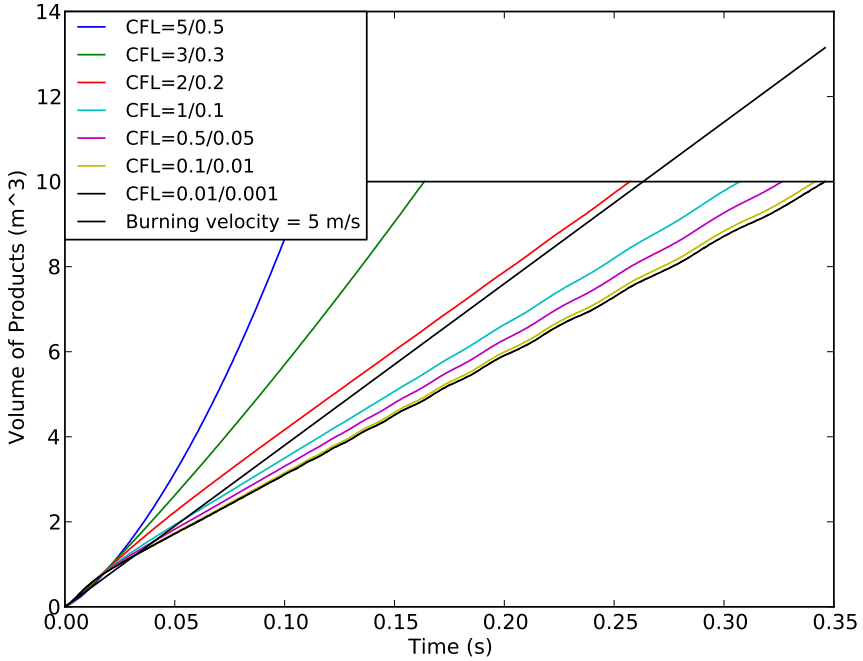

Figure 3.20: The result of variation of CFL values with the other parameters held constant, and with closed end ignition. The correction for long time steps is disabled, the burning velocity is set to 5 m/s and the grid cell size to 0.1 m. For decreasing CFL values, the flame speed is converging towards $\sim$ 28 m/s.

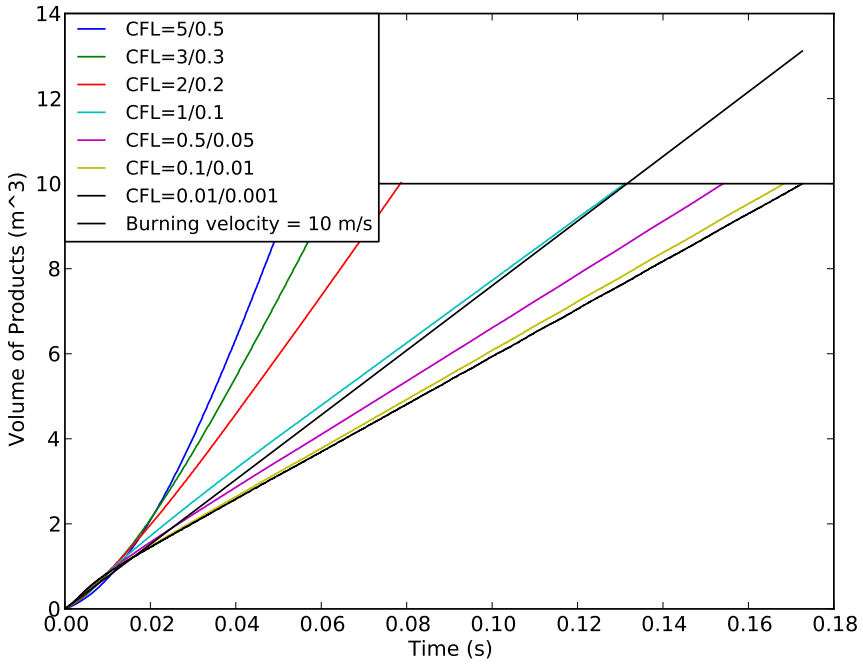

Figure 3.21: The result of variation of CFL values with the other parameters held constant, and with closed end ignition. The correction for long time steps is disabled, the burning velocity is set to 10 m/s and the grid cell size to 0.1 m. For decreasing CFL values, the flame speed is converging towards $\sim$ 56 m/s.

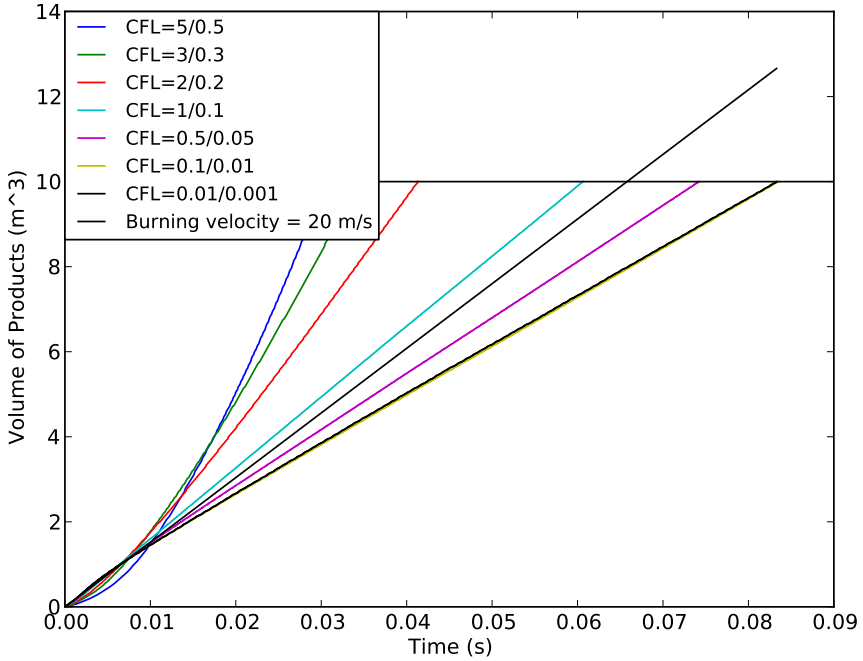

Figure 3.22: The result of variation of CFL values with the other parameters held constant, and with closed end ignition. The correction for long time steps is disabled, the burning velocity is set to 20 m/s and the grid cell size to 0.1 m. For decreasing CFL values, the flame speed is converging towards $\sim$ 117 m/s.

3.3.3.3 Numerical scheme effect

When the β model was implemented in FLACS, the van Leer numerical scheme was applied (Arntzen, 1998, p. 99). The current version of FLACS (10.1/10.2) utilises a κ scheme (GexCon AS, 2013, p. 342), and because of this, a set set of simulations were carried out to see if the change in numerical scheme could be a part of the explanation to why the flame speed is slower than expected. All the tests conducted with the van Leer scheme had the correction function enabled. The results from simulations with the burning velocity set to 5 m/s is shown in Figure 3.25. The van Leer scheme seems to give less deviation from the correct flame speed compared to the κ scheme. Similar results were also obtained for 10 m/s (Figure 3.26), and 20 m/s (Figure 3.27). The results are summarised in Table 3.4. Comparison of the flame thickness for the simulation with burning velocity of 10 m/s, and CFLC/CFLV=2/0.2 is shown in Figure 3.24. The area under the van Leer graph is $0.1(0.05 + 0.83 + 1.30 + 0.99 + 0.64) = 0.38$, while the area under the κ graph is $0.1(0.12 + 1.44 + 1.06 + 0.41) = 0.30$. This means that the κ flame will burn $(0.38 - 0.3)/0.3 \approx 27$ % slower than the van Leer flame in this case, something that agrees well with the resulting flame speeds. In the same manner as for the other closed end ignition simulations, Fo values were plotted against the deviation from the correct flame speed in Figure 3.23. The same trend as for the rest of the closed end ignition simulations was observed here as well, with convergence at Fo values below 0.003.

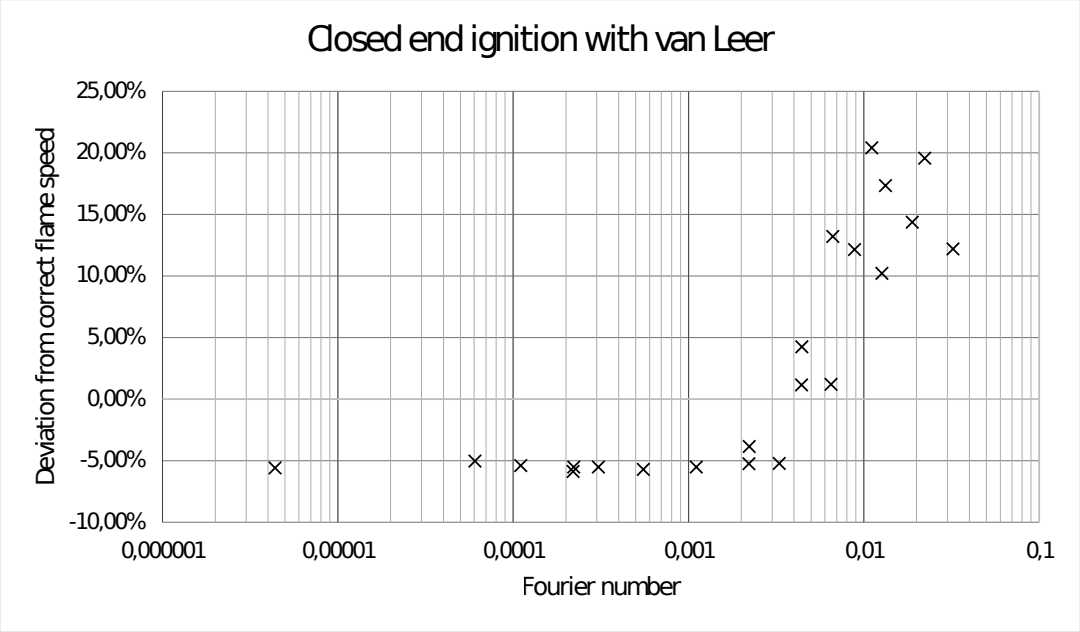

Figure 3.23: Deviation from the correct flame speed as a function of the Fourier number for closed end ignition with the β model, the correction function enabled, and with the van Leer numerical scheme.

Table 3.4: Convergence results from closed end ignition with van Leer numerical scheme

Velocity (m/s)					
Input	S_f with expansion	CFLC	CFLV	Converged S_f (m/s)	Percent deviation
5	38	0.25	0.025	35.832	-5.71
10	76	0.05	0.005	71.741	-5.87
20	152	0.05	0.005	143.620	-5.51

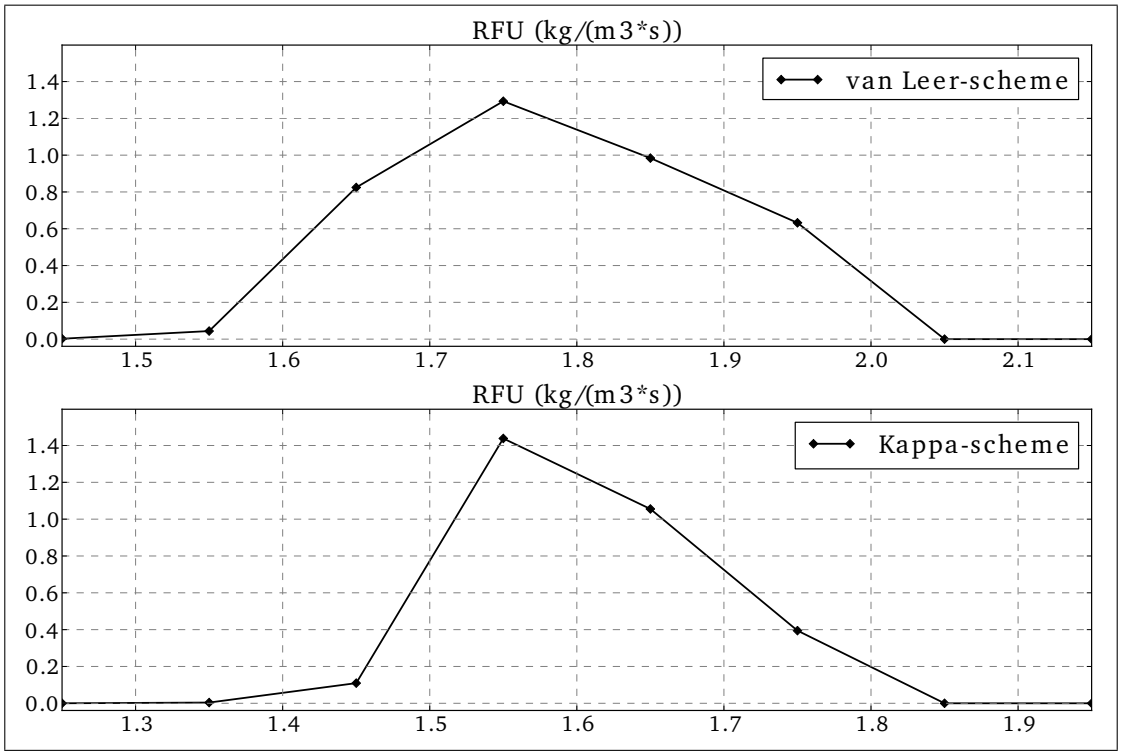

Figure 3.24: Comparison of the flame thickness with van Leer, and κ. The van Leer flame has reaction in five grid cells, while the κ flame has reaction in four cells.

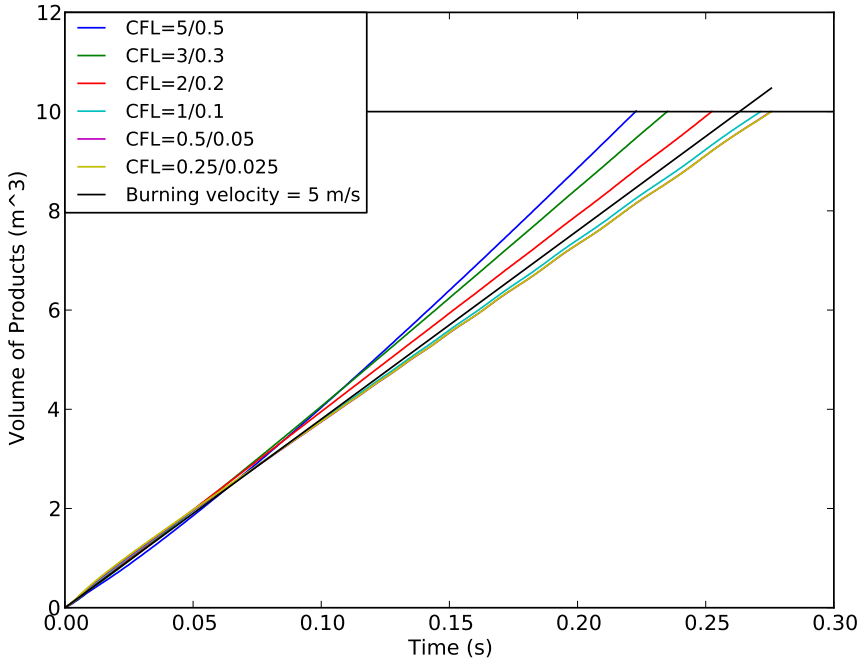

Figure 3.25: The result of variation of CFL values with the other parameters held constant, and with closed end ignition. The numerical scheme is set to van Leer, the burning velocity is set to 5 m/s and the grid cell size to 0.1 m. For decreasing CFL values, the flame speed is converging towards $\sim$ 36 m/s

.

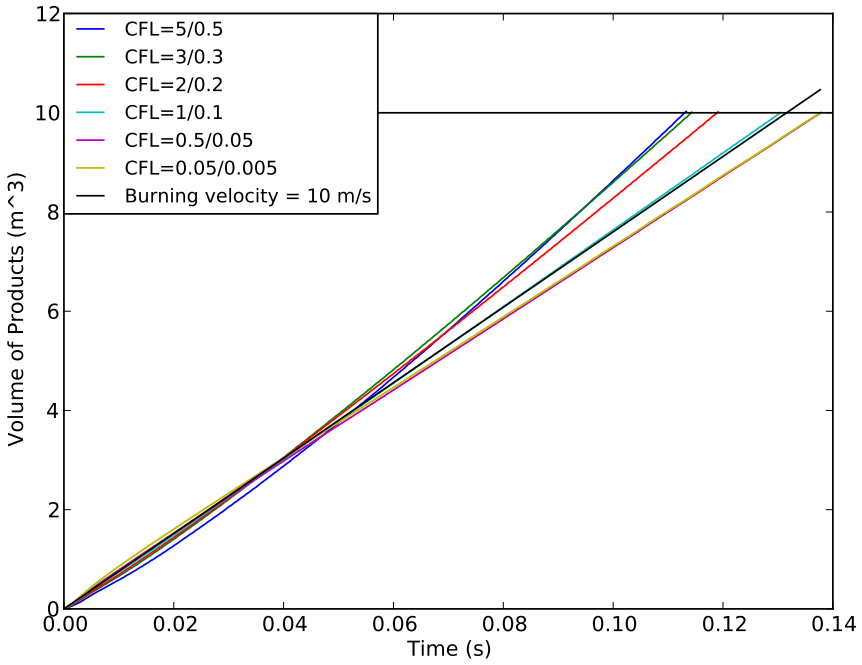

Figure 3.26: The result of variation of CFL values with the other parameters held constant, and with closed end ignition. The numerical scheme is set to van Leer, the burning velocity is set to 10 m/s and the grid cell size to 0.1 m. For decreasing CFL values, the flame speed is converging towards $\sim$ 72 m/s

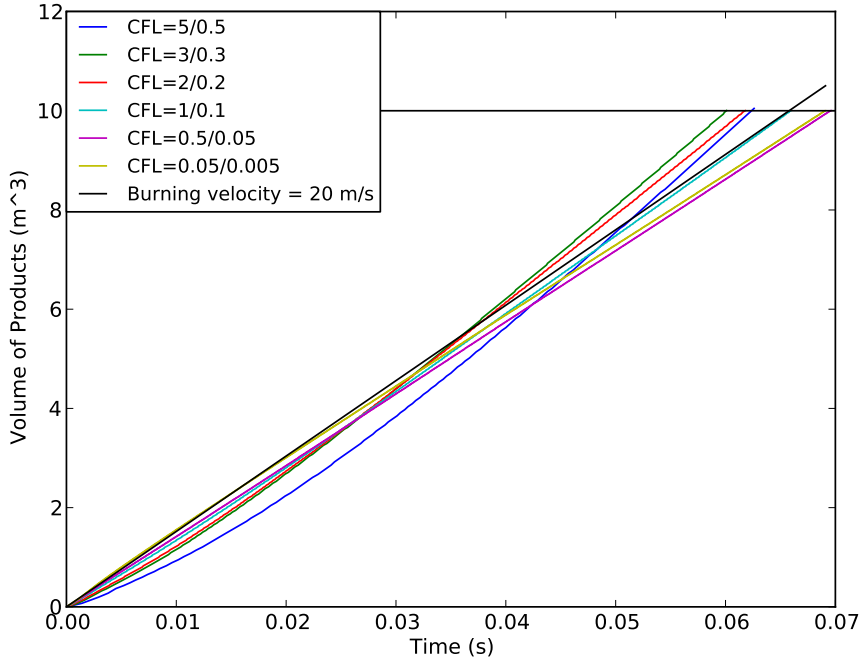

.

Figure 3.27: The result of variation of CFL values with the other parameters held constant, and with closed end ignition. The numerical scheme is set to van Leer, the burning velocity is set to 20 m/s and the grid cell size to 0.1 m. For decreasing CFL values, the flame speed is converging towards $\sim$ 144 m/s

.

3.4 Open end ignition with the β model

In the same manner as for closed end ignition, 1D numerical testing was conducted for the 10 m channel with ignition in the open end. Preliminary testing revealed that the most stable results were obtained without extra grid in the open end, and the rest of the cases were therefore simulated with the grid limited to the 10 m channel. Towards the end of the numerical experiments that comprises this research, some interesting results cast doubt about whether the closed end wall influenced the results too much. Some results and thoughts about the subject are presented in Section 3.7. Simulations were in the same way as for closed end ignition performed with and without the correction function described in Section 3.3.2.

As demonstrated later in this section, oscillations in the flame speed are frequently encountered in the open end ignition simulations. As a means to reduce the oscillations, the flame was artificially thickened by doubling the diffusion near the flame. This was achieved by multiplying the standard value of $\mathcal{D}$ in Equation 2.30 by a factor of two. The resulting flame thickness difference is shown in Figure 3.28. Results from simulations with normal flame thickness are presented in Sections 3.4.1.1 and 3.4.2.1. Results from simulations with double flame thickness are presented in Sections 3.4.1.2 and 3.4.2.2.

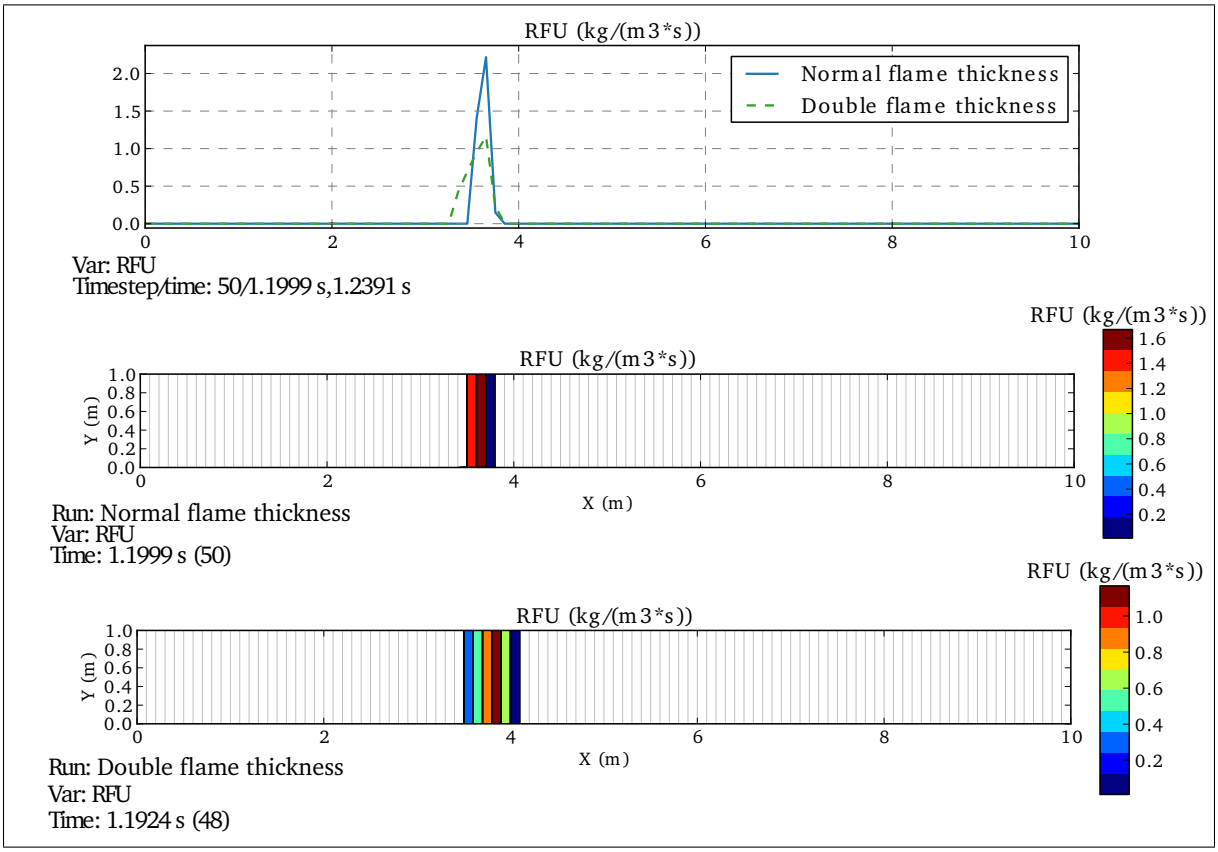

Figure 3.28: Combustion rate (RFU) with normal and double flame thickness.

3.4.1 Time step testing with correction

3.4.1.1 Normal flame thickness

Simulations were conducted with burning velocities of 5, 10, 20, and 30 m/s, and the correction function enabled (FLACS standard). For the simulation with burning velocity set to 5 m/s, the results lie close to expected flame speed (approximately 2 % too high velocity with the exception of the highest time step size). When the time step size is decreased, the flame speed starts to oscillate. The burning velocity was then set to 10 m/s, and the time steps varied. The resulting flame speeds were also here too high, and the spread between the different time step sizes increased in comparison to the 5 m/s results. S_f is approaching the correct value when the time step size is reduced, but increased oscillation is also observed. Burning velocities of 10 and 20 m/s, resulted in similar results as for the lower burning velocities. The flame speed is observed to be constant, and higher in the first $\sim$ 0.05 s of the simulation. This is consistent in all the four sets of simulations, but most prominent with the highest burning velocities. Values for Fo were calculated in the same manner as for closed end ignition, and the results are plotted against deviation from the correct flame speed in Figure 3.29. The trend is not as clear as for closed end ignition, but Fo values below 0.006 indicates convergence.

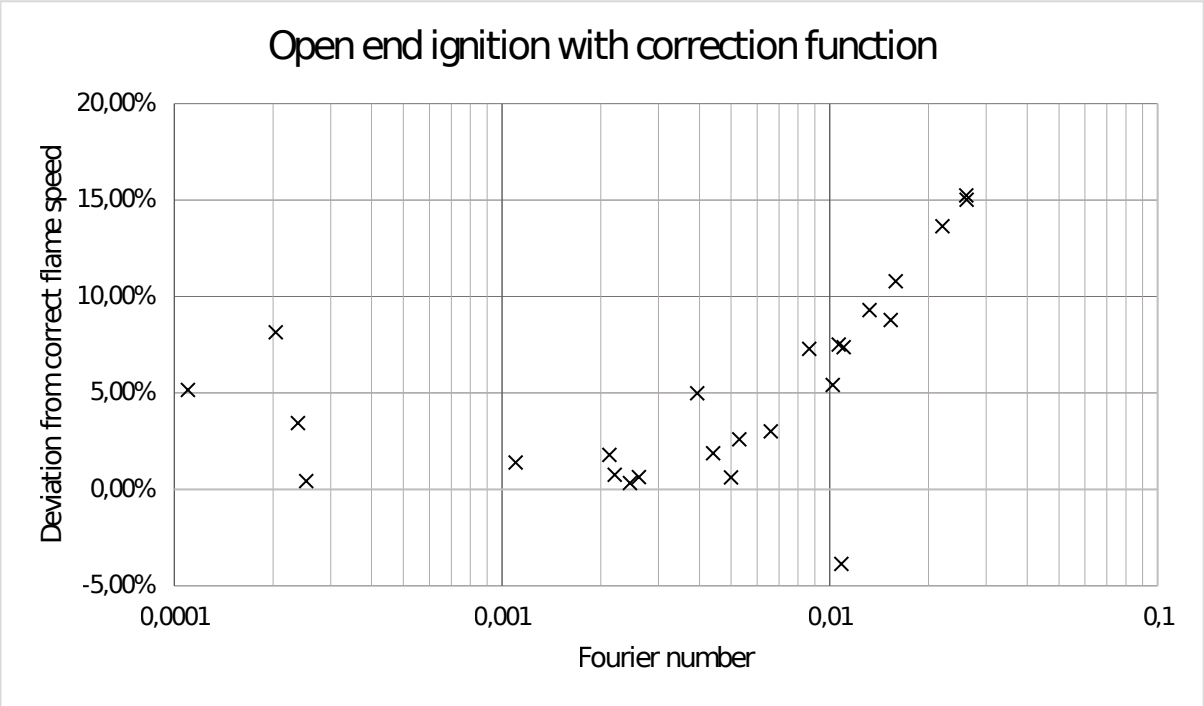

Figure 3.29: Deviation from the correct flame speed as a function of the Fourier number for open end ignition with the β model and the correction function enabled.

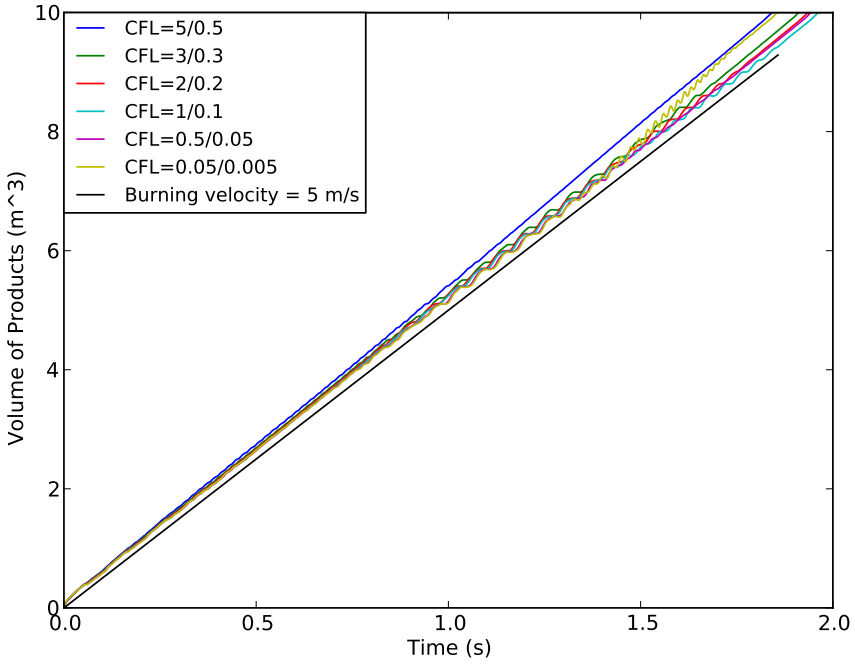

Figure 3.30: The result of variation of CFL values with the other parameters held constant, and with open end ignition. The burning velocity is set to 5 m/s, and the grid cell size to 0.1 m. S_f is $\sim$ 2 % too high, and for decreasing CFL values, the flame speed starts to oscillate.

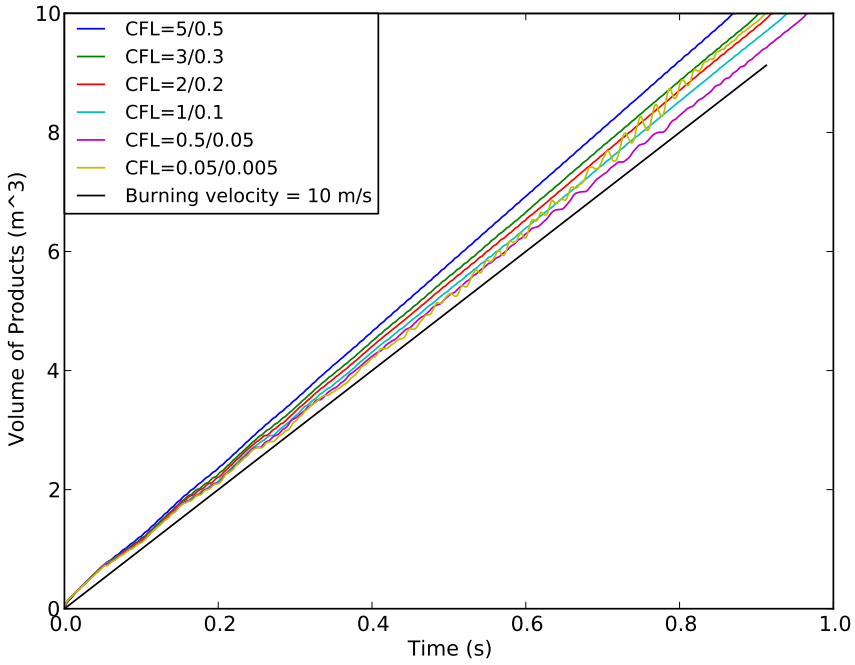

.

Figure 3.31: The result of variation of CFL values with the other parameters held constant, and with open end ignition. The burning velocity is set to 10 m/s, and the grid cell size to 0.1 m. S_f is $\sim$ 10-5 % too high, and for decreasing CFL values, the flame speed starts to oscillate.

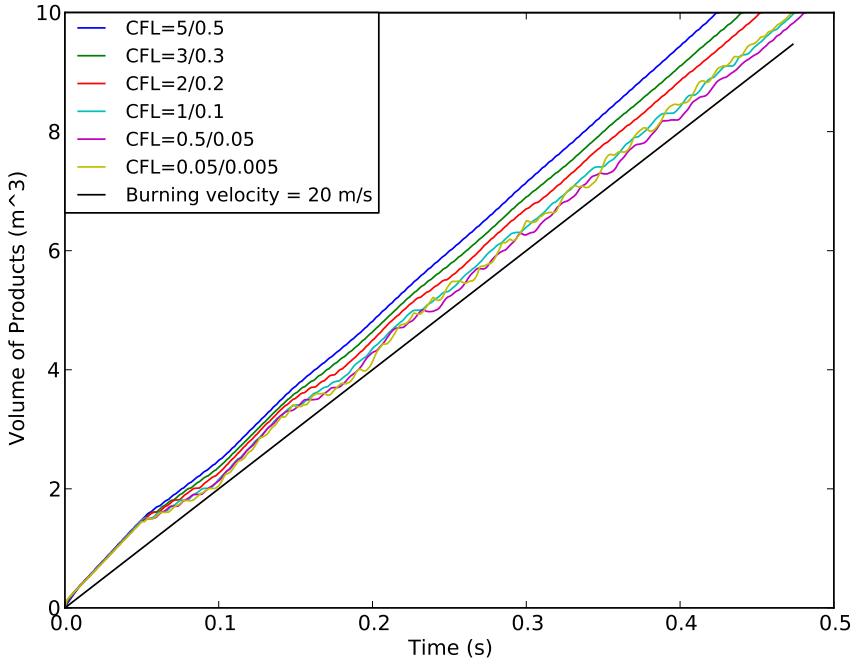

Figure 3.32: The result of variation of CFL values with the other parameters held constant, and with open end ignition. The burning velocity is set to 20 m/s, and the grid cell size to 0.1 m. S_{f} is $\sim$ 15-5 % too high, and for decreasing CFL values, the flame starts to oscillate.

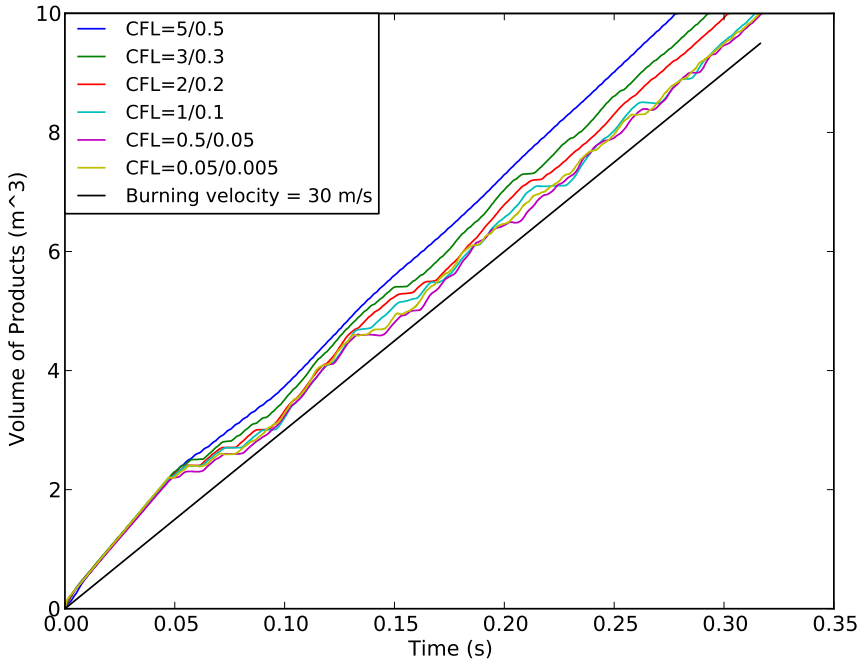

Figure 3.33: The result of variation of CFL values with the other parameters held constant, and with open end ignition. The burning velocity is set to 30 m/s, and the grid cell size to 0.1 m. S_{f} is $\sim$ 15-0.5 % too high, and for decreasing CFL values, the flame starts to oscillate.

3.4.1.2 Double flame thickness

Identical cases as with normal flame thickness in Section 3.4.1.1 were simulated with the diffusion near the flame doubled. The results are presented in Figures 3.35 to 3.38. The simulations with the burning velocity set to 5 m/s resulted in more stable flame speeds than the corresponding simulations with normal flame thickness, and the deviations from the correct flame speed were also in the same range (6-1 % too high). For the burning velocities of 10, 20 and 30 m/s, the same trend was observed. The deviations from the correct flame speed for these burning velocities were however less than for the simulations with normal flame thickness (11-1.5 %). Values for Fo are calculated and plotted against deviation from the correct flame speed in Figure 3.34. Simulations with Fo below 0.006 converges towards values with a deviation of $\sim$ 1.5 %

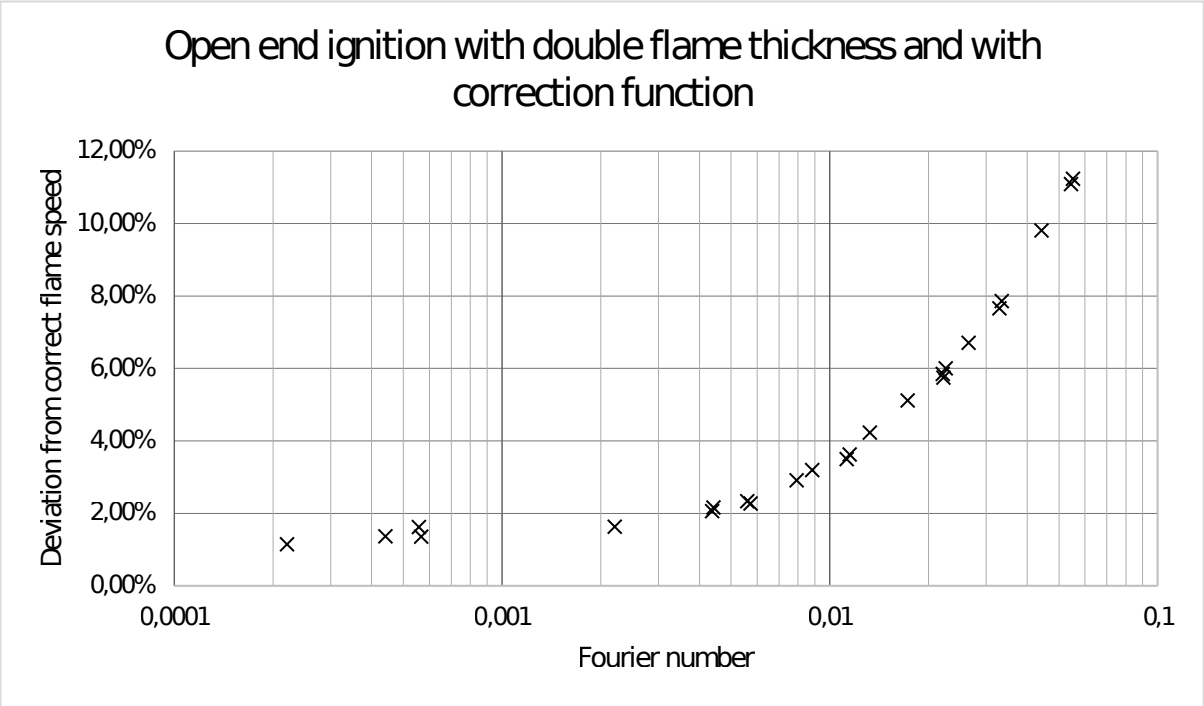

Figure 3.34: Deviation from the correct flame speed as a function of the Fourier number for open end ignition with the β model,the correction function enabled and with double flame thickness.

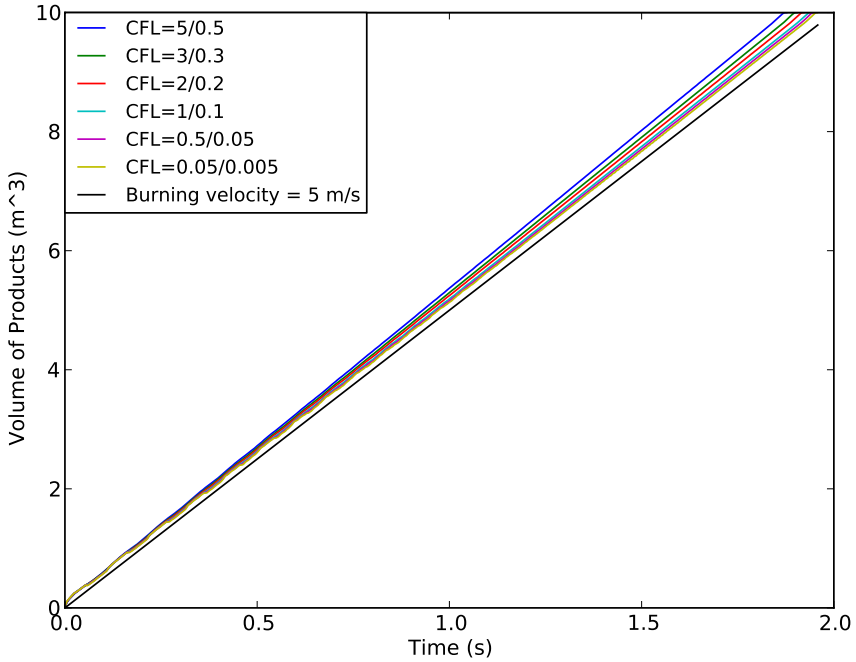

Figure 3.35: The result of variation of CFL values with the other parameters held constant, and with open end ignition. The burning velocity is set to 5 m/s, the flame thickness is doubled, and the grid cell size set to 0.1 m.

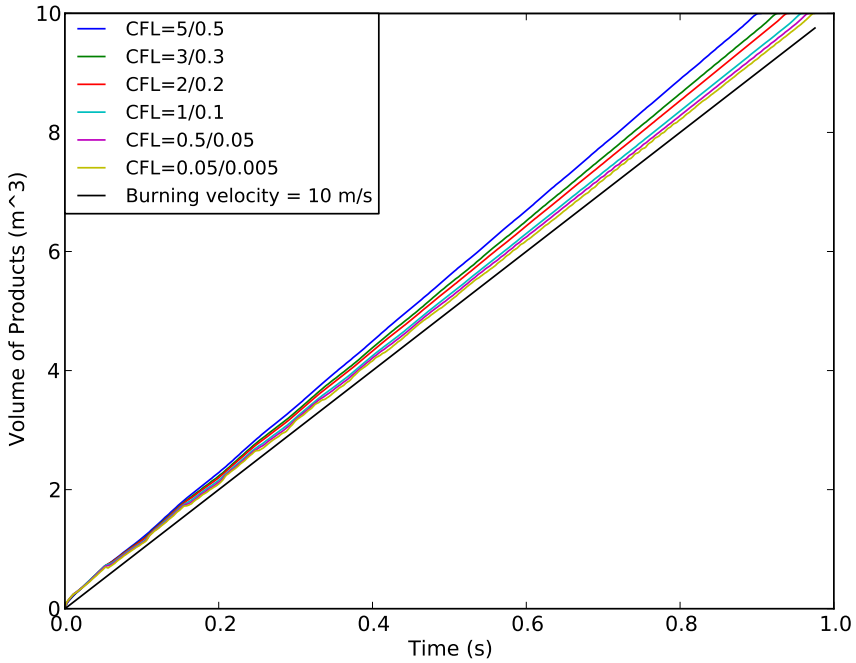

Figure 3.36: The result of variation of CFL values with the other parameters held constant, and with open end ignition. The burning velocity is set to 10 m/s, the flame thickness is doubled, and the grid cell size set to 0.1 m.

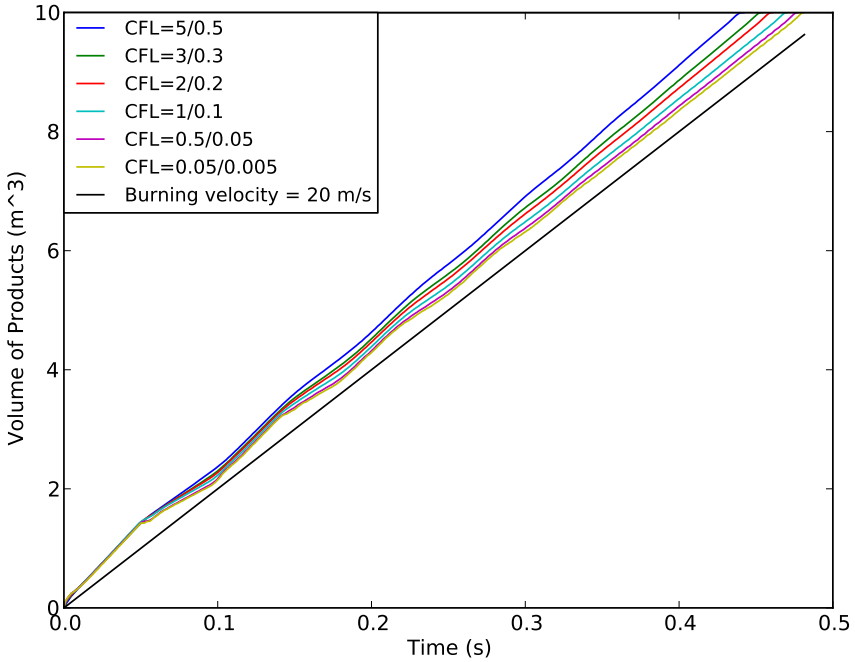

Figure 3.37: The result of variation of CFL values with the other parameters held constant, and with open end ignition. The burning velocity is set to 20 m/s, the flame thickness is doubled, and the grid cell size set to 0.1 m.

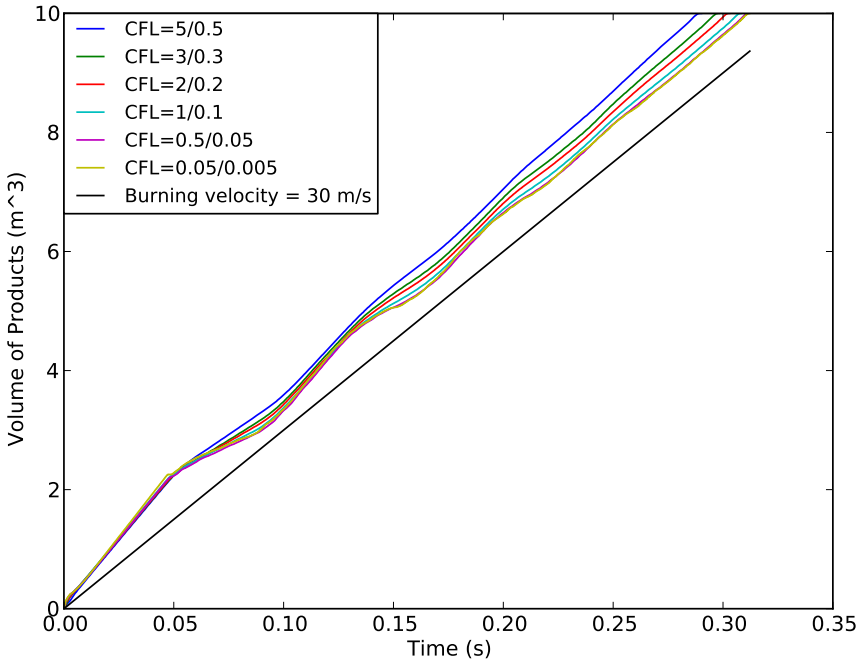

Figure 3.38: The result of variation of CFL values with the other parameters held constant, and with open end ignition. The burning velocity is set to 30 m/s, the flame thickness is doubled, and the grid cell size set to 0.1 m.

3.4.2 Time step testing without correction

3.4.2.1 Normal flame thickness

The same set of burning velocities as in Section 3.4.1 was tested with the correction function disabled. Results from the simulations are presented in Figures 3.40 to 3.43. The tests with burning velocity set to 5 m/s resulted in S_f values with < 1 % deviation from the theoretical value. With the lowest CFLC/CFLV values used (0.05/0.005), some deviating oscillations were observed after ~ 1.5 s. When the burning velocity was further increased to 10 m/s, the deviation from the correct S_f was still small, but increased to < 2 % deviation. Similar to the former simulations, the lowest time step size did also here result in a deviating oscillation after ~ 0.5 s, see Figure 3.41. A burning velocity of 20 m/s gave similar result, with maximum deviation from the correct value < 2 %. However, as seen in Figure 3.42, no deviating oscillations were observed at the lowest time step. At a burning velocity of 30 m/s, a moderate amount of oscillation occurred, and the deviation from the correct flame speed was observed to be $\sim -2\%$. As seen in Figure 3.43, no oscillation that dramatically changes the flame speed was observed at low time step sizes. It is however worth noticing that even though the flame speed is rather constant throughout the simulation, fluctuations in the flame speed is observed when it is plotted against time. This is shown in Figure 3.44. The Fourier number results are presented in Figure 3.39. No clear trend was observed, but most of the results lie within ± 2 %.

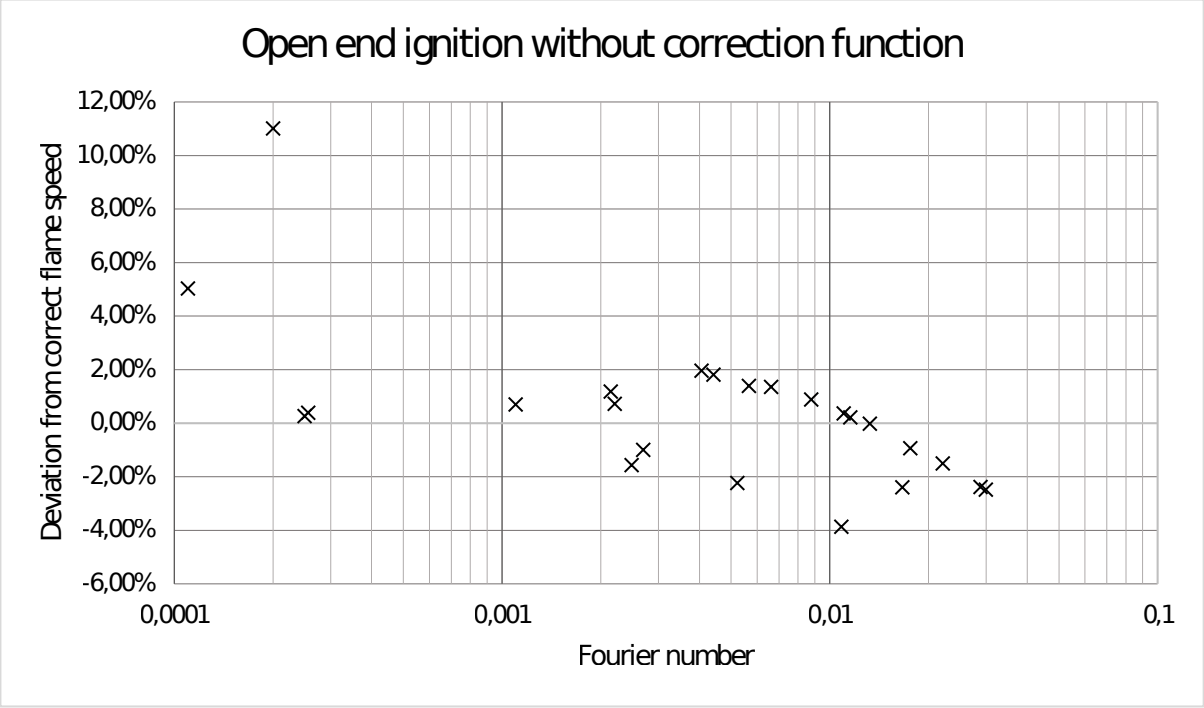

Figure 3.39: Deviation from the correct flame speed as a function of the Fourier number for open end ignition with the β model and the correction function disabled.

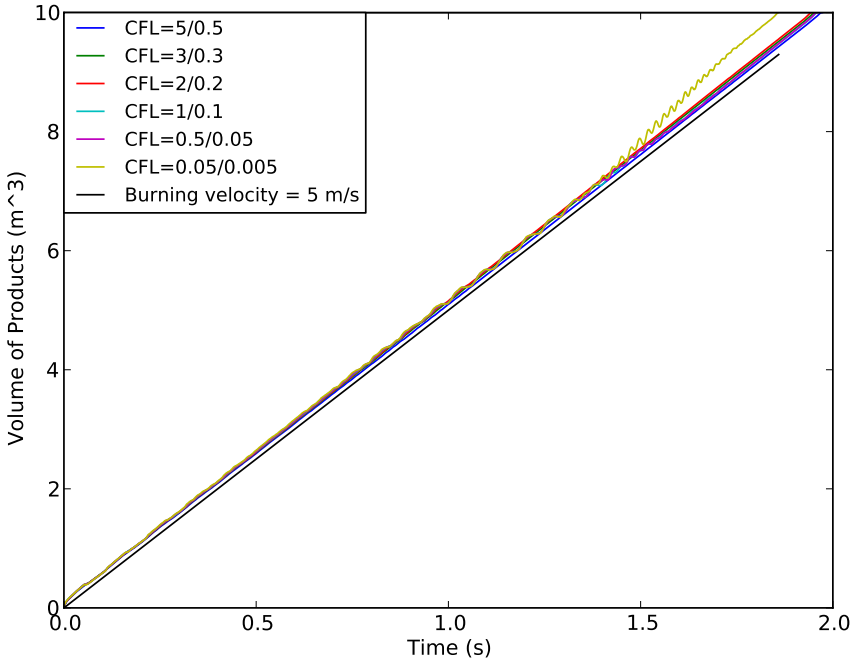

Figure 3.40: The result of variation of CFL values with the other parameters held constant, and with open end ignition. The correction for long time steps is disabled, the burning velocity is set to 5 m/s, and the grid cell size to 0.1 m.

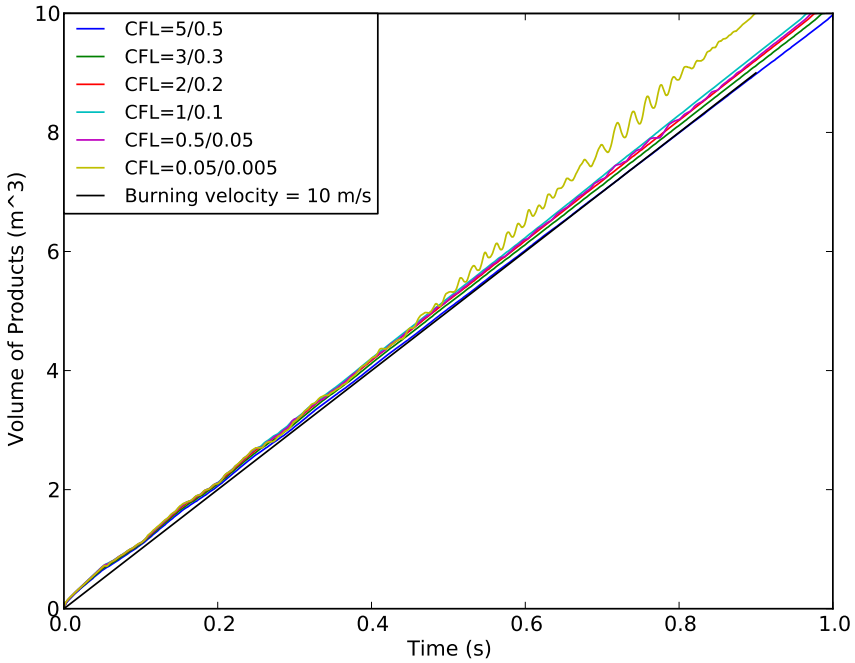

Figure 3.41: The result of variation of CFL values with the other parameters held constant, and with open end ignition. The correction for long time steps is disabled, the burning velocity is set to 10 m/s, and the grid cell size to 0.1 m.

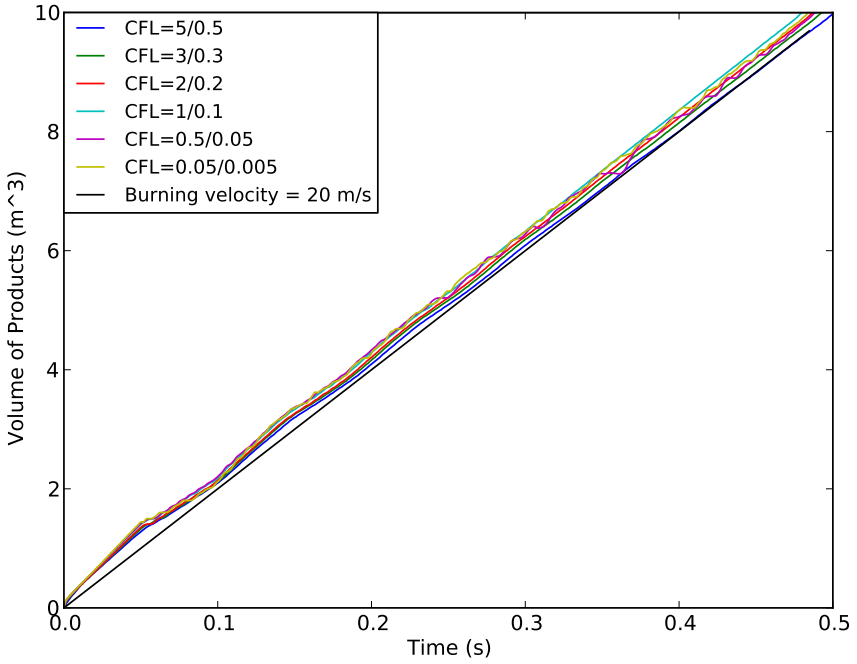

Figure 3.42: The result of variation of CFL values with the other parameters held constant, and with open end ignition. The correction for long time steps is disabled, the burning velocity is set to 20 m/s, and the grid cell size to 0.1 m.

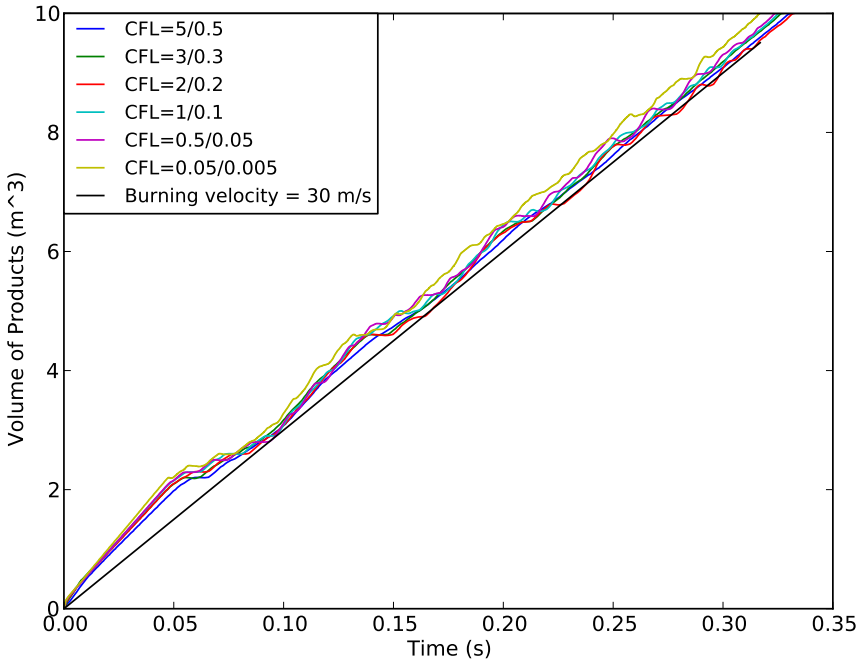

Figure 3.43: The result of variation of CFL values with the other parameters held constant, and with open end ignition. The correction for long time steps is disabled, the burning velocity is set to 30 m/s, and the grid cell size to 0.1 m.

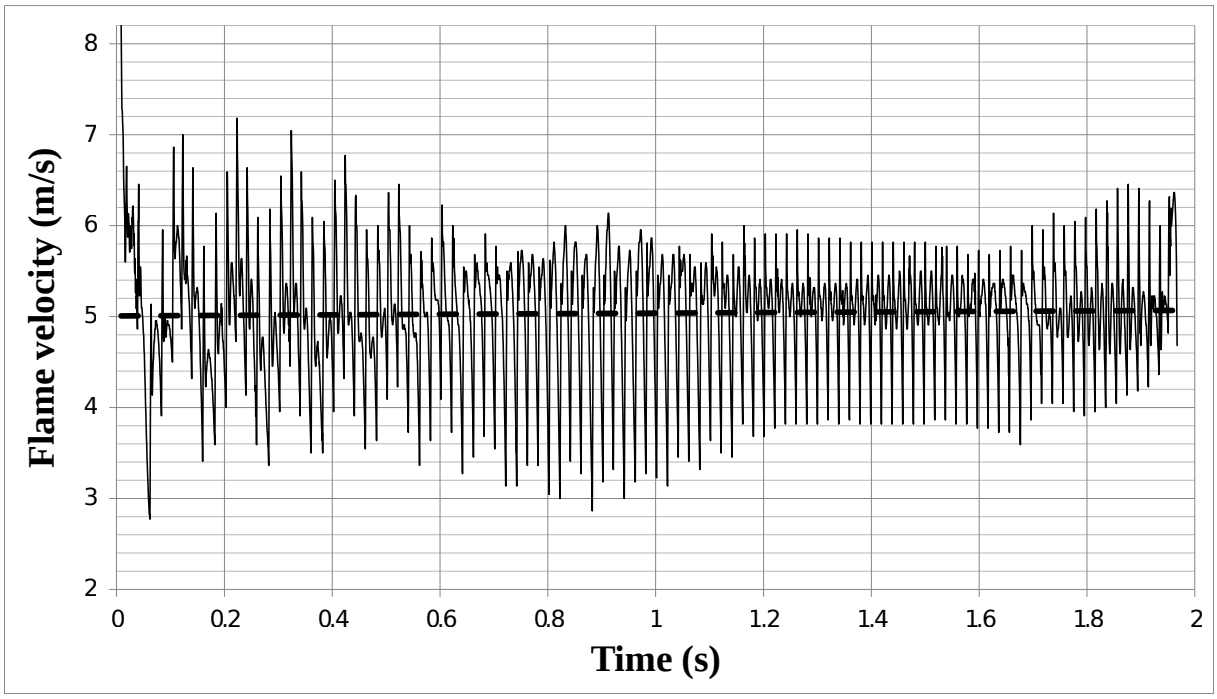

Figure 3.44: Velocity plot for burning velocity set to 5 m/s, CFLC/CFLV set to 5/0.5, and the correction function disabled. The dashed line represent the linear trend during the simulation.

3.4.2.2 Double flame thickness

Identical cases as with normal flame thickness in Section 3.4.2.1 were simulated with the diffusion near the flame increased by a factor of two. The results are presented in Figures 3.46 to 3.49. For the cases with the burning velocity set to 5 m/s, the resulting S_f values were in the range of 0.5 to 1 % deviation from the correct value. Variation in the time step size did not lead to notable changes. The same results were obtained for 10 m/s, but in this case the deviation varied between -0.1 to 1 %. When the burning velocity was further increased to 20 m/s, some oscillations were observed, but the mean velocity was still within ±1 %. The highest burning velocity gave more noticeable oscillations, but still around the correct value by a margin of ±1.5 %. Values for Fo plotted against the deviation from the correct flame speeds are presented in Figure 3.45. Values for Fo below 0.006 gives convergence.

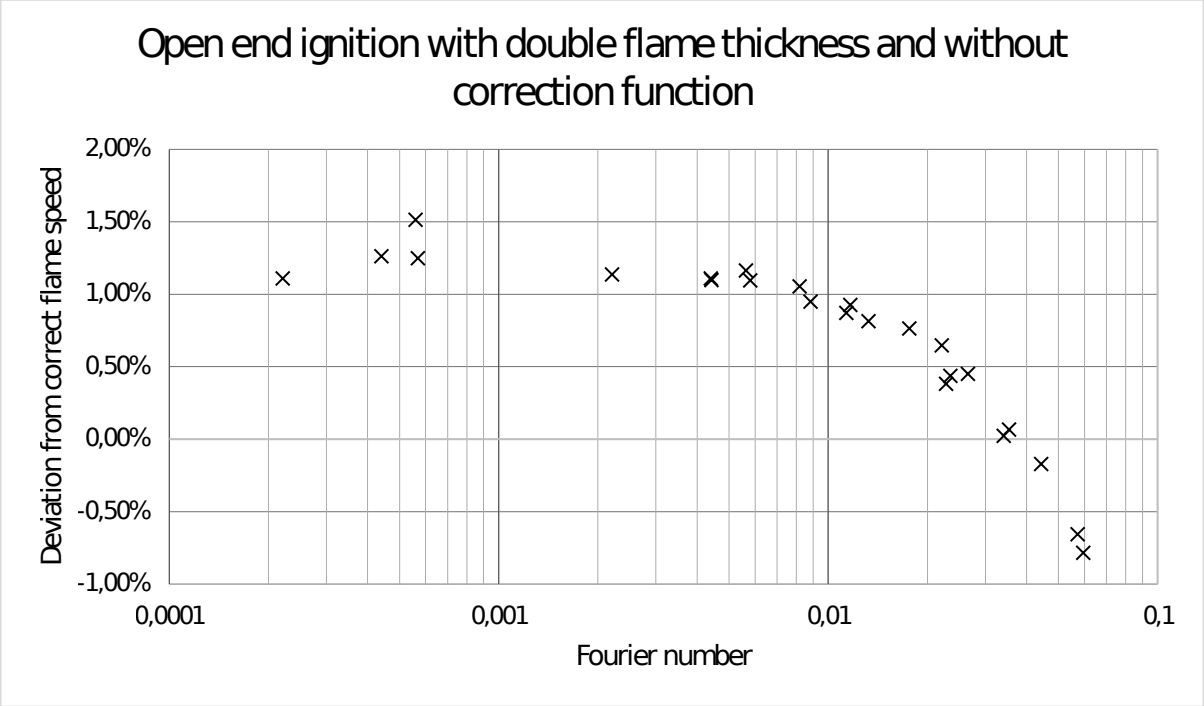

Figure 3.45: Deviation from the correct flame speed as a function of the Fourier number for open end ignition with the β model, the correction function disabled, and double flame thickness.

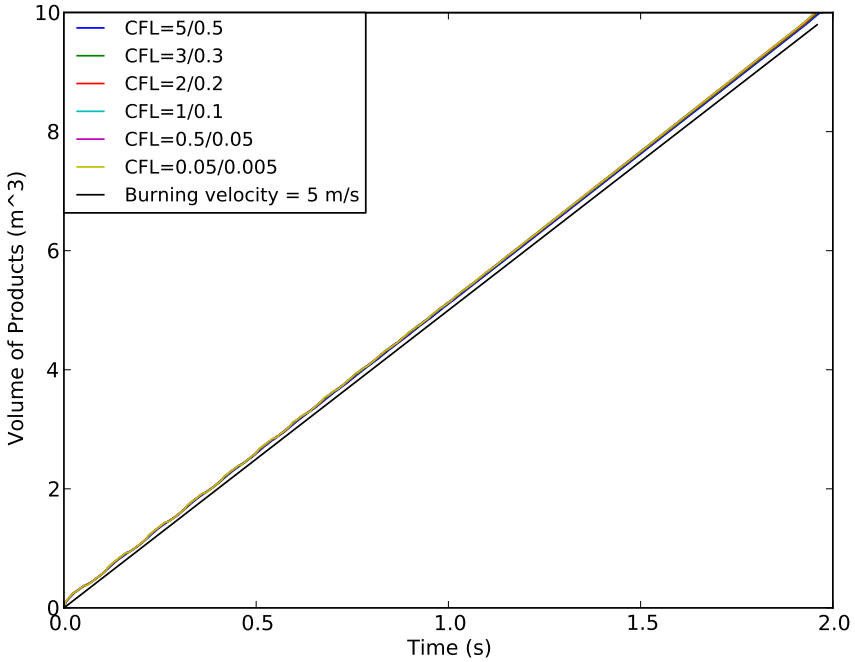

Figure 3.46: The result of variation of CFL values with the other parameters held constant, and with open end ignition. The correction for long time steps is disabled, the flame thickness is doubled, the burning velocity is set to 5 m/s, and the grid cell size to 0.1 m.

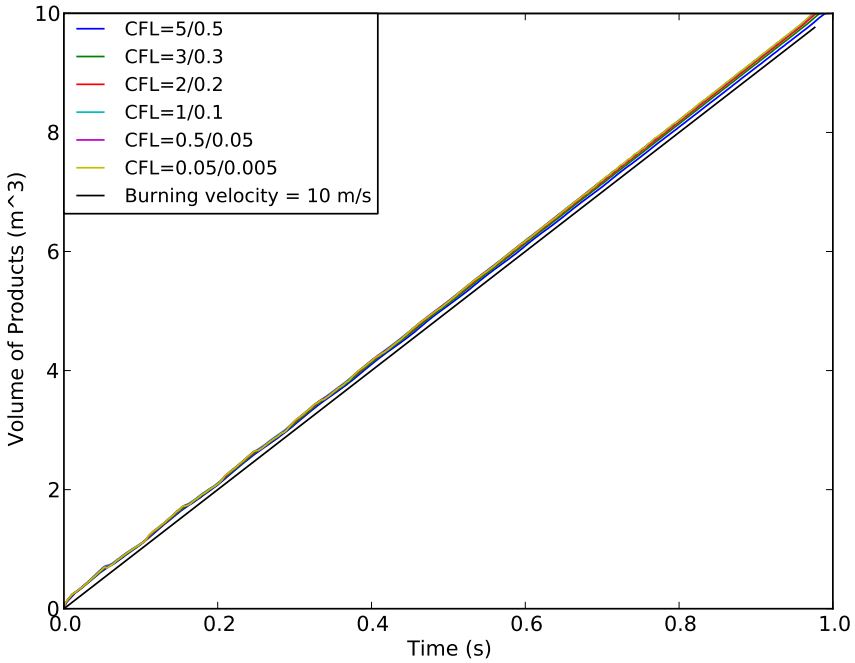

Figure 3.47: The result of variation of CFL values with the other parameters held constant, and with open end ignition. The correction for long time steps is disabled, the flame thickness is doubled, the burning velocity is set to 10 m/s, and the grid cell size to 0.1 m.

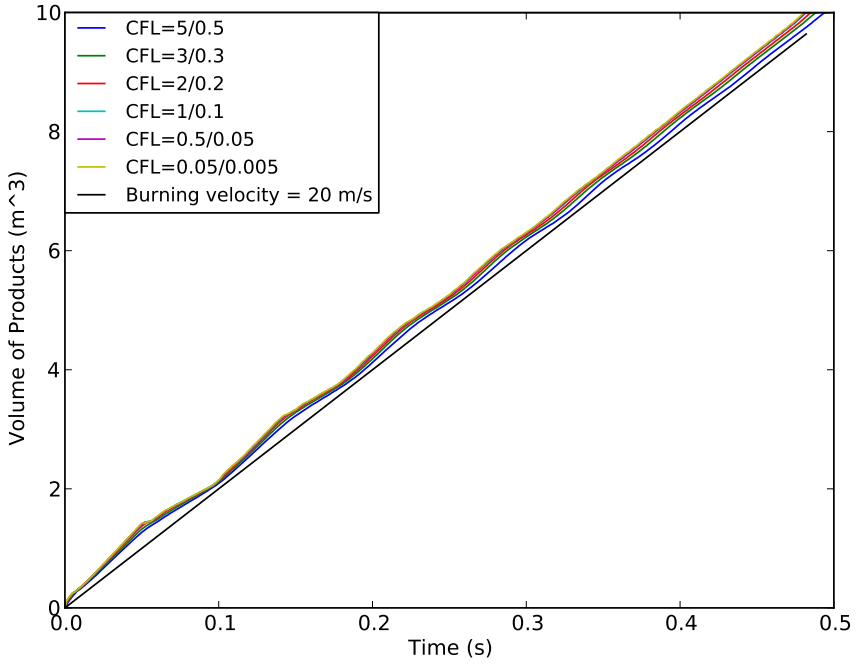

Figure 3.48: The result of variation of CFL values with the other parameters held constant, and with open end ignition. The correction for long time steps is disabled, the flame thickness is doubled, the burning velocity is set to 20 m/s, and the grid cell size to 0.1 m.

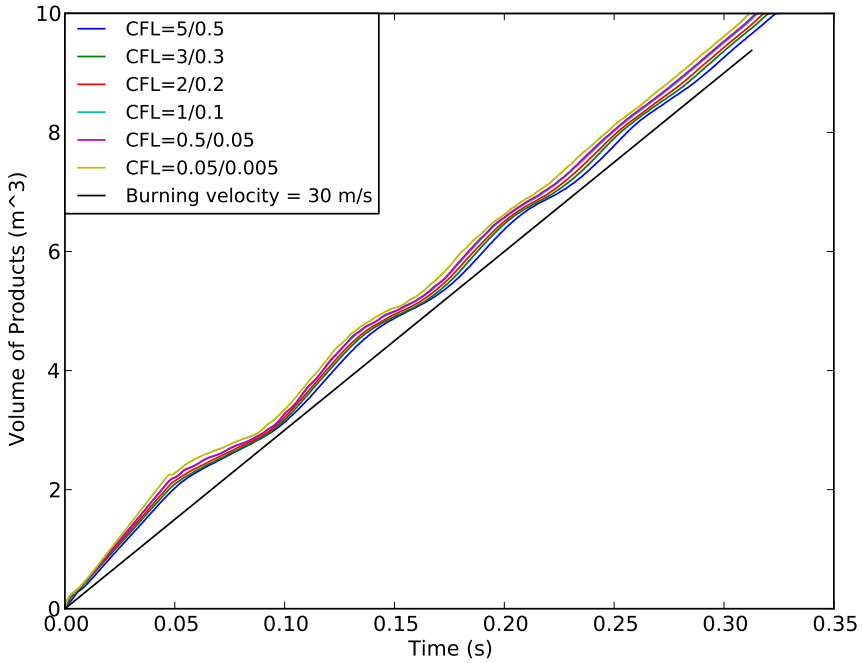

Figure 3.49: The result of variation of CFL values with the other parameters held constant, and with open end ignition. The correction for long time steps is disabled, the flame thickness is doubled, the burning velocity is set to 30 m/s, and the grid cell size to 0.1 m.

3.5 Closed end ignition with SIF

The combustion model SIF was additionally tested on the numerical channel for closed end ignition. The setup was equal to the setup in Section 3.3, and the results are presented in Figures 3.50 to 3.54. Due to good initial results with SIF, the tests were also run with CFLC/CFLV values of 10/1. For the simulations with a burning velocity of 0.67 m/s, the resulting S_f values deviated with less than -0.07 % from the correct value. No significant difference was observed when the time step size was varied. The simulations with a burning velocity of 2.6 m/s gave similar results, though a bit higher deviations, but still less than -0.5 %. Further increasing the burning velocity to 5 m/s increased the spread between results from different time steps. Nevertheless, all the results still deviated with less than ~ -1.5 % from the correct flame speed. At burning velocity of 10 m/s, further spread between the results were observed, especially the results from CFL=10/1. The highest time step size resulted in a deviation of -3.9 %, while lowering the time step size reduced the deviation from ~ -3 % to ~ -0.3 %. As seen in Figure 3.54, when the burning velocity was increased to 20 m/s, CFL=10/1 resulted in a strongly deviating flame speed at almost -38 %. The spread in the rest of the results varied between deviations of -6.6 % to -1.9 %. This is further discussed in Chapter 4. To sum up the results for the different burning velocities tested with closed end ignition; SIF provided accurate results, with little variation between the different time step sizes.

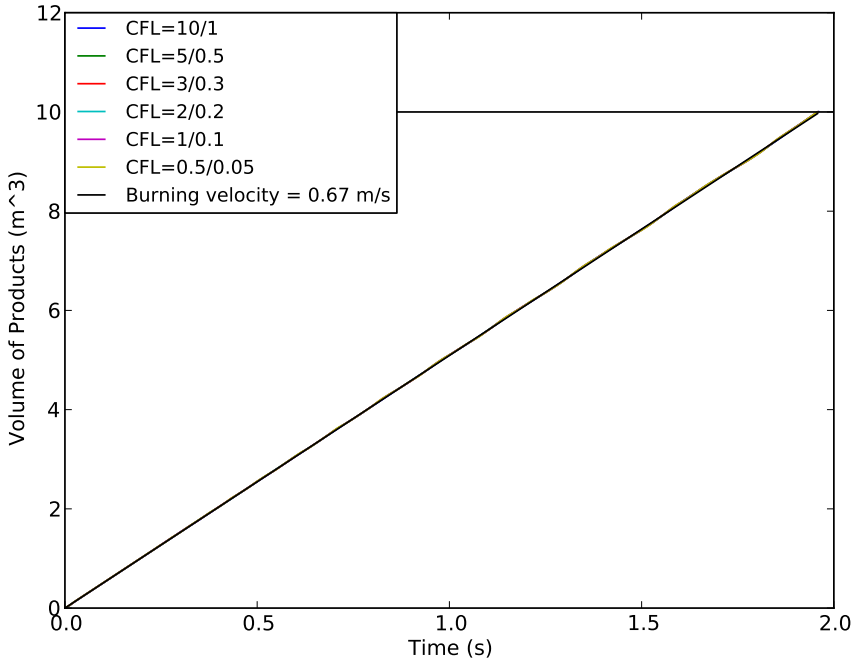

Figure 3.50: The result of variation of CFL values with the other parameters held constant, and closed end ignition. The combustion model is SIF, the burning velocity is set to 0.67 m/s, and the grid cell size to 0.1 m.

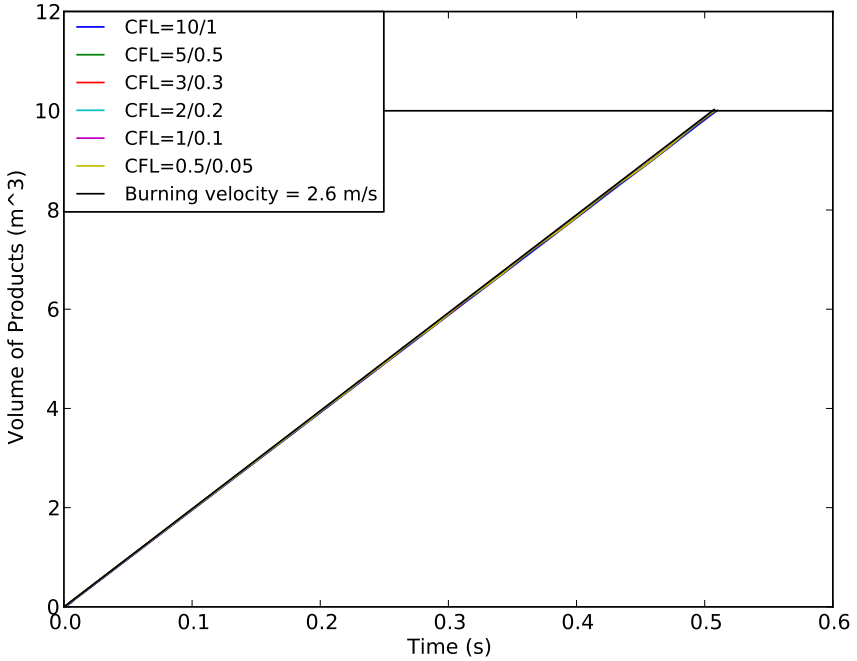

Figure 3.51: The result of variation of CFL values with the other parameters held constant, and closed end ignition. The combustion model is SIF, the burning velocity is set to 2.6 m/s, and the grid cell size to 0.1 m.

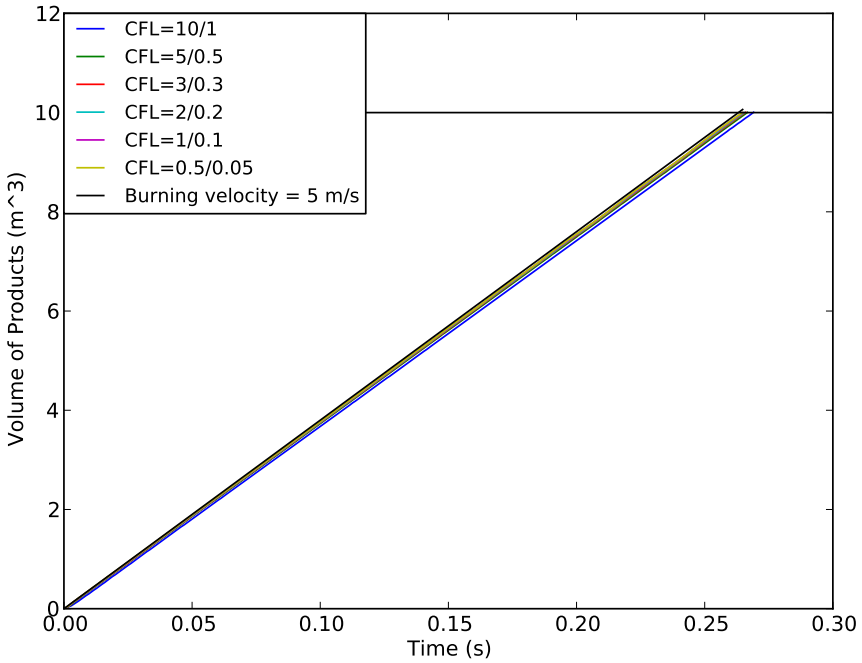

Figure 3.52: The result of variation of CFL values with the other parameters held constant, and closed end ignition. The combustion model is SIF, the burning velocity is set to 5 m/s, and the grid cell size to 0.1 m.

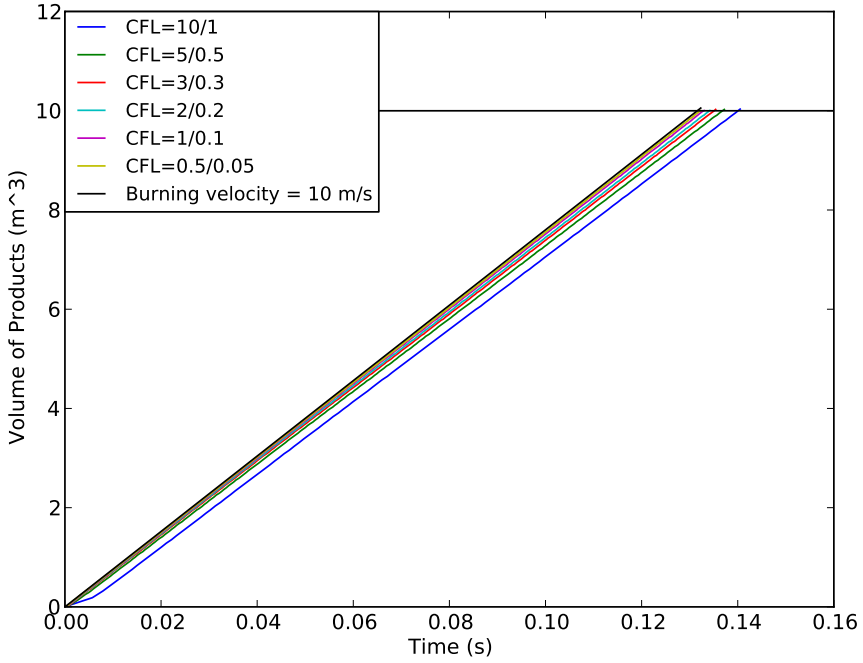

Figure 3.53: The result of variation of CFL values with the other parameters held constant, and closed end ignition. The combustion model is SIF, the burning velocity is set to 10 m/s, and the grid cell size to 0.1 m.

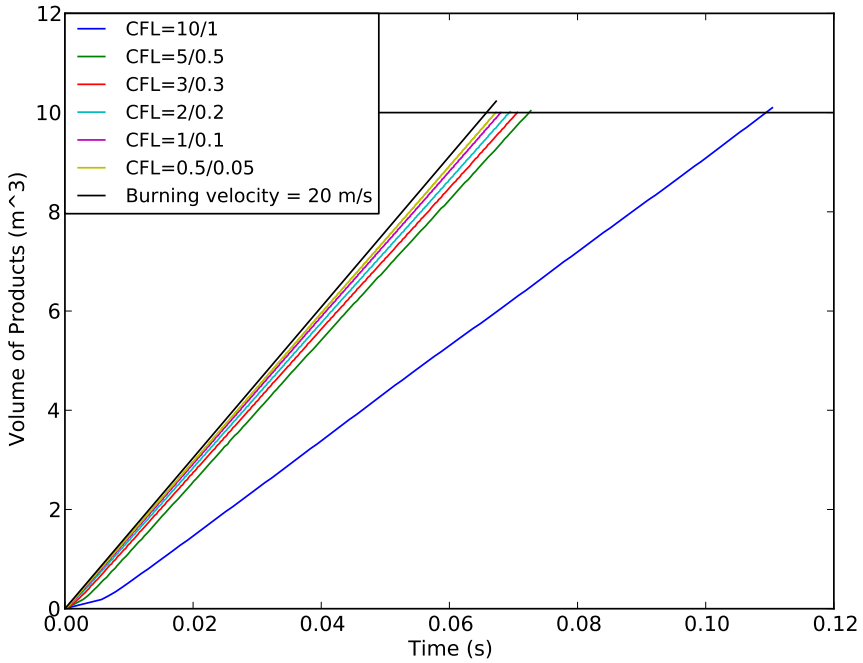

Figure 3.54: The result of variation of CFL values with the other parameters held constant, and closed end ignition. The combustion model is SIF, the burning velocity is set to 20 m/s, and the grid cell size to 0.1 m.

3.6 Open end ignition with SIF

The combustion model SIF was furthermore tested on the numerical channel for open end ignition. The setup was equal to the setup in Section 3.4, and the results are presented in Figures 3.55 to 3.58. At the lowest burning velocity, good agreement between the results and the correct flame speed is observed. No significant spread between the results were observed, and the deviations from the correct flame speed were less than 0.2 %. Increasing the burning velocity to 10 m/s resulted in oscillations for the shortest time step sizes. The mean velocities did however deviate from the correct flame speed with less than 0.8 %. At burning velocity of 20 m/s, even stronger oscillations occurred, and the flame speeds deviated with $2-3$ % from the correct value. Further increasing the burning velocity to 30 m/s resulted in similar oscillations as for 20 m/s, and the deviations from the correct flame speed increased to $5-6$ %. The observed oscillations are a result of flow pattern changes due to compression effects in the reactants ahead of the flame. This phenomena is more closely explained in Section 3.7.1.

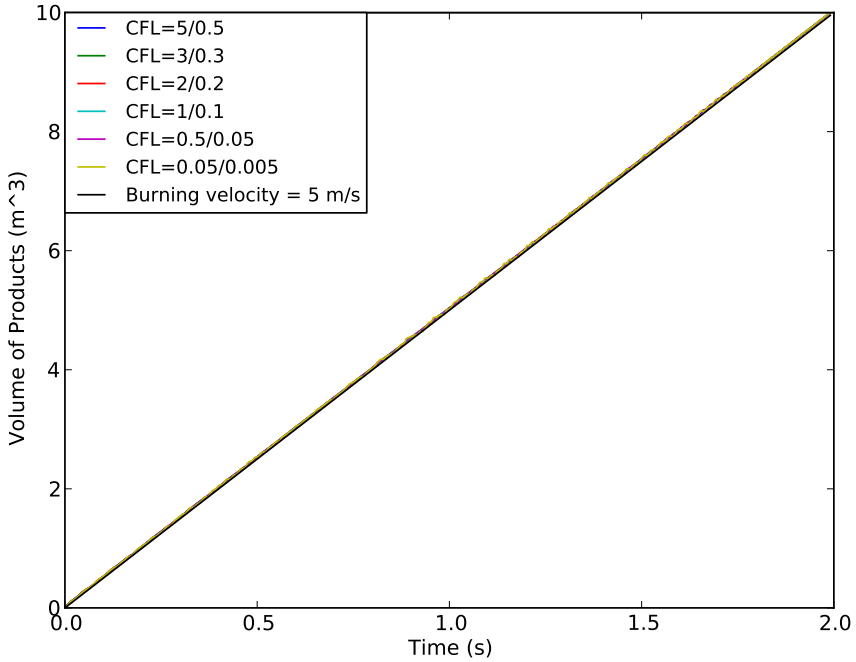

Figure 3.55: The result of variation of CFL values with the other parameters held constant, and open end ignition. The combustion model is SIF, the burning velocity is set to 5 m/s, and the grid cell size to 0.1 m.

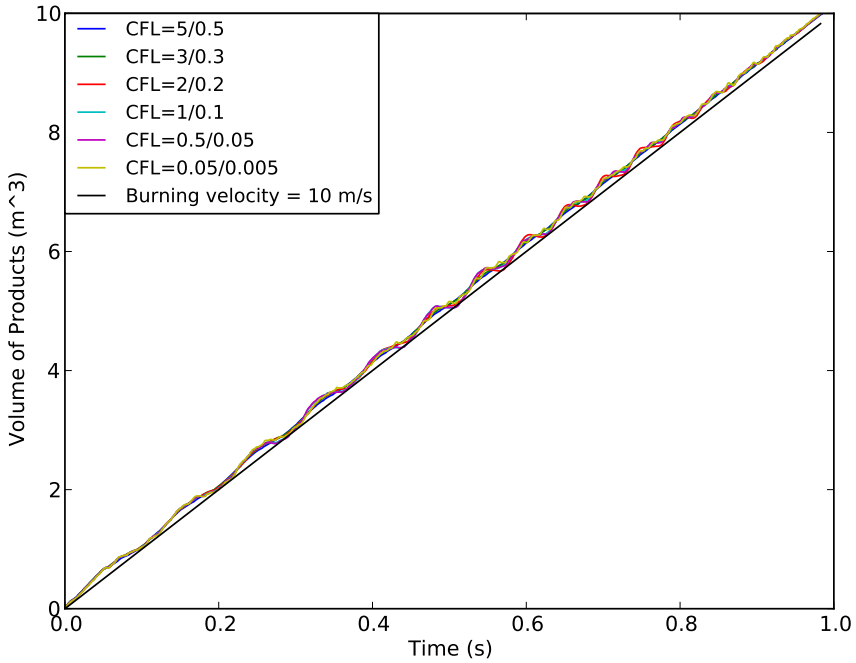

Figure 3.56: The result of variation of CFL values with the other parameters held constant, and open end ignition. The combustion model is SIF, the burning velocity is set to 10 m/s, and the grid cell size to 0.1 m.

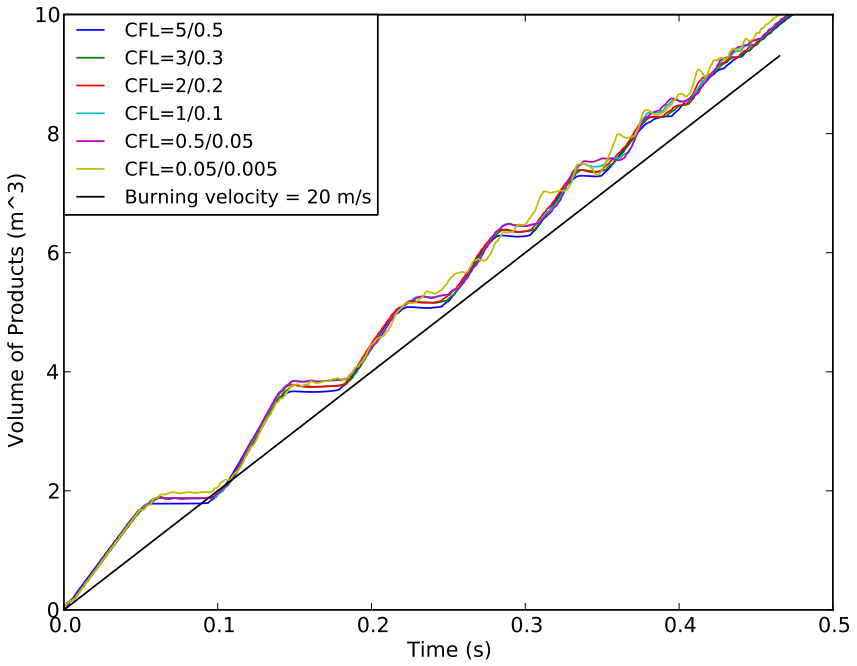

Figure 3.57: The result of variation of CFL values with the other parameters held constant, and open end ignition. The combustion model is SIF, the burning velocity is set to 20 m/s, and the grid cell size to 0.1 m.

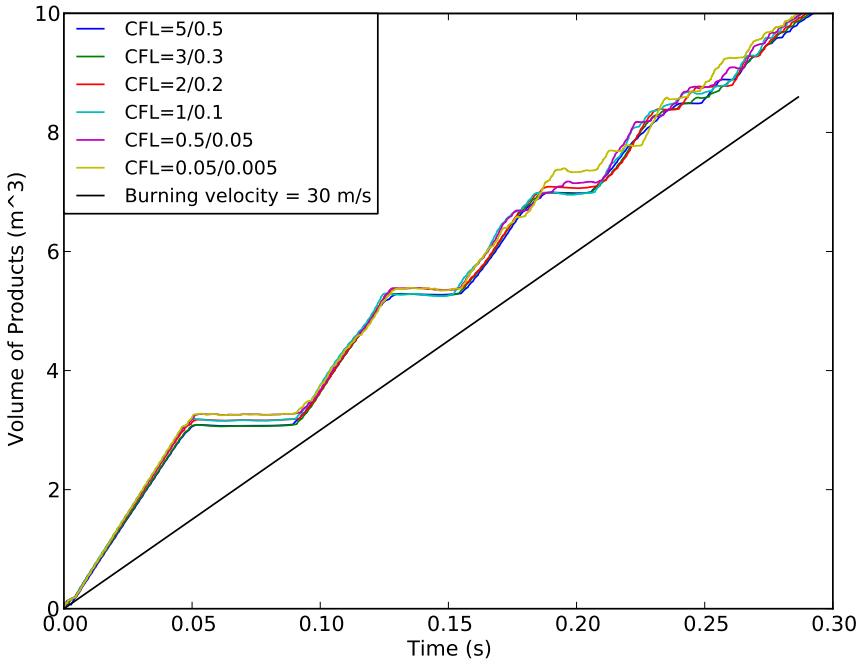

Figure 3.58: The result of variation of CFL values with the other parameters held constant, and open end ignition. The combustion model is SIF, the burning velocity is set to 30 m/s, and the grid cell size to 0.1 m.

3.7 Boundary effect for open end ignition

Towards the end of this research, it was discovered that the closed end wall of the channel had a greater impact on simulation results than previously anticipated. The channel was therefore extended as shown in Figure 3.59. Due to the limited time frame from this finding to submission of this research, only a selection of simulations were done with the long channel.

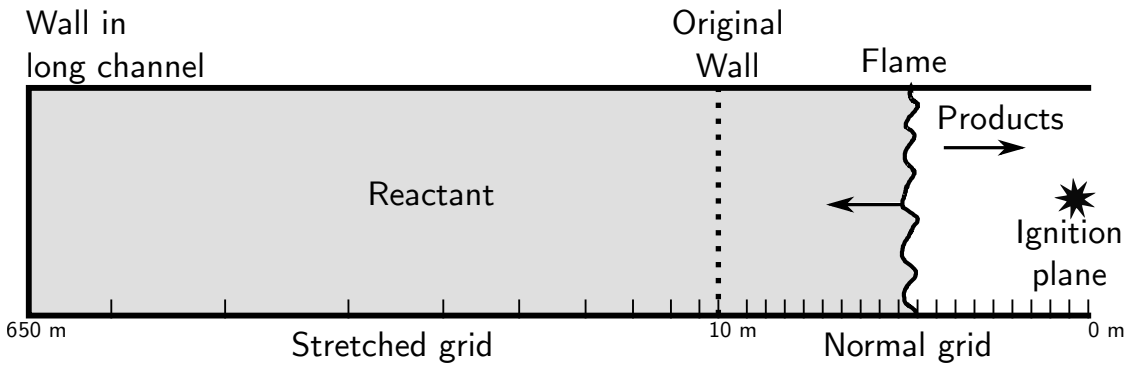

Figure 3.59: The extended channel used for open end ignition simulations in Section 3.7. The channel used in earlier simulations was limited to the volume from the "Original wall" to the open end.

3.7.1 SIF

Increasing the distance to the wall for open end ignition had a great impact on the results with SIF. Variation between different time step sizes did, as in Section 3.6 not result in large changes in the burning velocity. The mean flame speeds encountered when the wall is moved further away from the ignition point are however much higher than when the channel is closed at 10 m. This is illustrated by a comparison of the different flame speeds to their corresponding correct flame speeds in Figure 3.60. The high flame speed observed in the simulations with the long channel, were also observed periodically in the simulations with the short channel. Since the onset of changes to the flame speed was at $\sim$ 0.05 s, it was considered to be an effect of pressure reflection from the closed end wall. This was also the motivation for extending the channel. Comparison of flow velocities for the similar cases with long and short channel revealed that compression from the pressure wave caused by the flame front, give rise to enough compression in the reactants to result in flow towards the closed end of the channel. This is equal for both the long and the short channel, but in the case of the short channel, the flow is reversed due to the close proximity to the wall, causing flow towards the flame. This is shown in Figure 3.61. The flame speed observed in the long channel with a burning velocity of 20 m/s was $\sim$ 34.8 m/s, and subtracting the flow ahead of the flame yields:

$$S = S_{\mathrm{f}} - U = 34.8 - 14.6 = 20.2 \text{ m/s} \tag{3.9}$$

The flame speed relative to the gas is therefore close to the correct value, and the deviation of the flame speed is not due to problems with the flame model, but a result of the physics involved

in the simulation. The same applies to the simulations with the short channel (Section 3.6). In the first 0.05 s, the flame is burning in reactants that move away from the flame (ahead of it). When the flow is reversed, in the case of the 20 m/s burning velocity, the flow approaches the flame at ~ 20.4 m/s, effectively keeping the flame stationary, or even pushing it back, before the pressure gradient causes the flow to reverse once more. As the flame is approaching the closed end wall, time between the flow reversals will decrease.

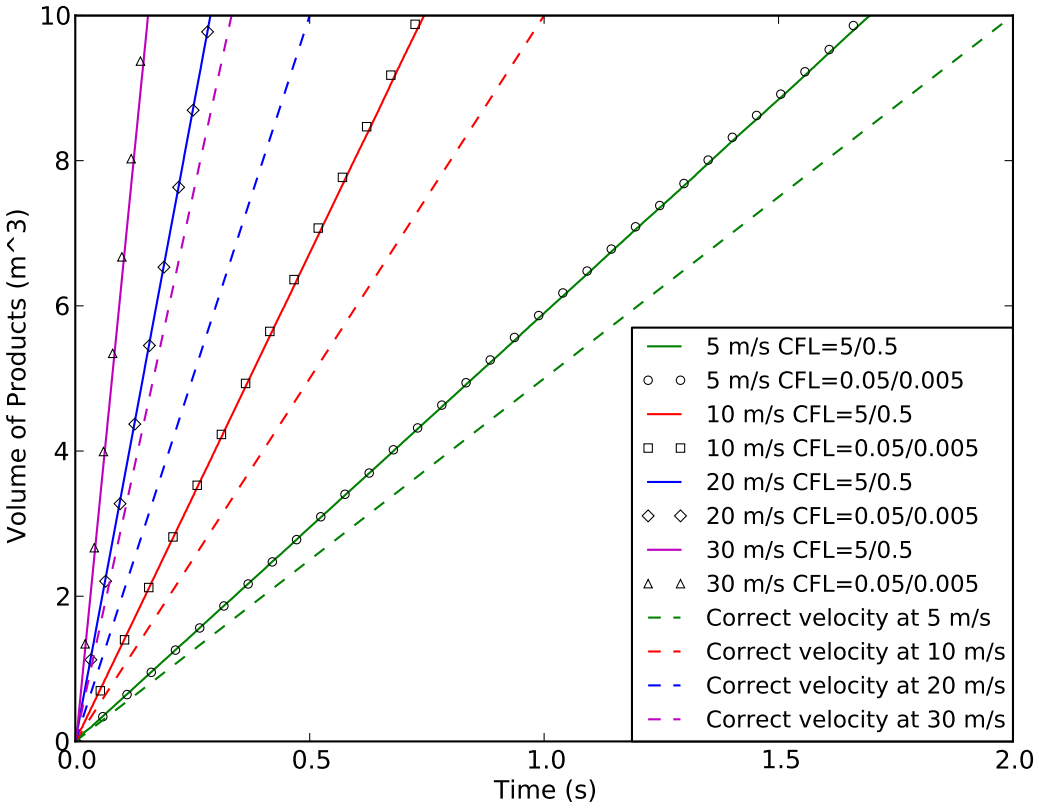

Figure 3.60: Results from variation of CFL values, at different burning velocities for open end ignition. The combustion model is SIF, the channel is 650 m long, with a grid cell size of 0.1 m the first 10 m.

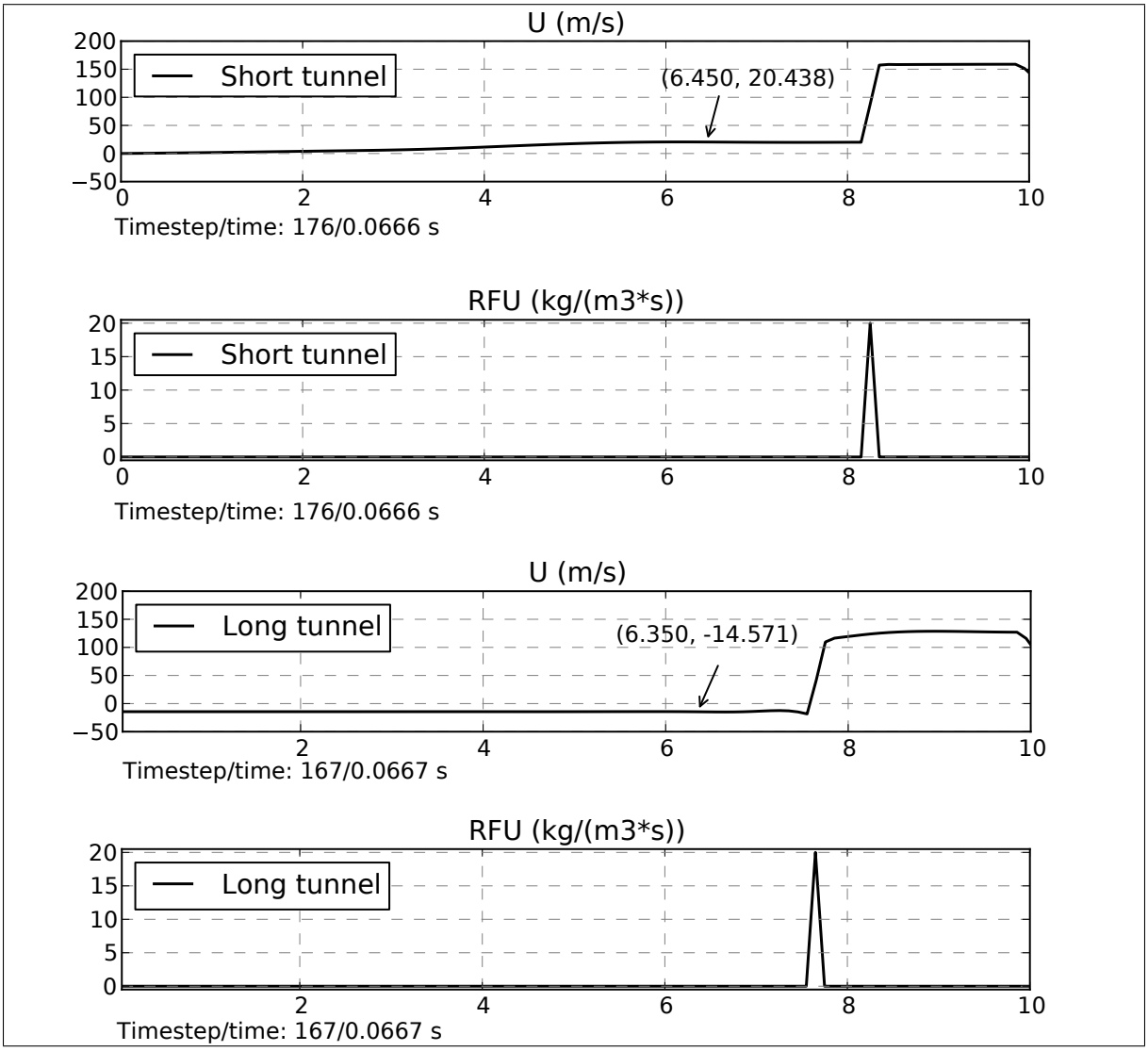

Figure 3.61: The flow pattern for the short and the long channel after $\sim$ 0.067 s, with a burning velocity of 20 m/s, ignition in open end.

Chapter 4

Discussion

The first subject for discussion is the choice of method for measuring the flame speed. As the volume of products depends on the pressure/density, pressure fluctuations will have a great influence on the time plot. Even though effects like turbulence, wall functions, and gravity are turned off, the system handles the rest of the physics included in FLACS. Pressure wave propagation is naturally a part of physics, but nonphysical effects need to be filtered out. The boundaries in FLACS have great influence on the results, and ideally the boundaries should be located away from the combustion. Since the boundaries define the numerical channel used in this research it is however not possible to completely avoid them. Regardless of the pressure effects, the volume of products method should give an accurate description of how fast the flame is moving.

4.1 β model closed end ignition

The consistent trend for closed end ignition with the β model, is flame speed convergence towards a too low value. As seen in Table 3.2 and 3.3; the deviation is also in the same range for all the simulations, at ~ -27 %. Both the simulations with time step correction function enabled and disabled experiences the convergence towards the low value. As the correction function only should be active with long time steps, this is as expected, since the convergence occurs at short time steps. Simulations were also conducted with the previously used van Leer numerical scheme, and the resulting flame speeds from these simulations were considerably closer to the correct values. From Table 3.4, it is clear that the flame speed converges towards a value ~ 6 % lower than the correct flame speed. Comparing the flame thickness of two identical cases, but with the two different numerical schemes, it is clear that the reaction zone is larger with van Leer, compared to the κ scheme. This can be seen in Figure 3.24, and the reaction rate of fuel in the case of van Leer is ~ 27 % higher than for the κ scheme. This is probably due to less numerical diffusion with the κ scheme. Normally this is a good thing, but since the β model was adjusted to work with the van Leer scheme, less numerical diffusion leads to a too slow flame. Several parameters can be adjusted to increase the flame speed in FLACS, and some of these values have probably been adjusted to correct for the burning velocity. An adjustment may be made in the β model, so that the reduction in numerical diffusion is compensated for.

4.2 β model open end ignition

The simulations with open end ignition generally gives flame speeds close to the correct values. The simulations with the correction function turned off, did however result in less deviation between the different time step sizes, and also flame speeds closer to the correct value. Due to the close proximity of the closed end wall, the open end ignition simulations are to a great extent influenced by pressure effects, and reflection from the wall. Compression in the reactants causes flow towards the closed end wall, and after a short time a reversal off the flow, i.e. flow towards the flame. This forward/back motion, causes the oscillation in the flame speed. In an attempt to reduce the oscillations, the flame thickness was doubled. The oscillations with short wavelengths were effectively filtered out, while the oscillations with the longest wavelengths remained. The drawback of double flame thickness is that a ~ 5 grid cells thick flame is too thick for practical use, unless the grid cell size is small.

4.3 SIF closed end ignition

The results for closed end ignition with SIF were in good agreement with the expected values. However, at a burning velocity of 20 m/s, and at CFLC/CFLV values at 10/1, the flame speed deviated strongly. This highlights a problem that can arise with high flame speeds for SIF. With the SIF flame model, the flame can only propagate one grid cell in each time step. In each time step, the flame is moved to the surrounding cells, if all the reactants in the cell is converted to products. This implies that the time steps need to be small enough in order to restrict the flame from moving more than one grid cell in each time step. As mentioned in the beginning of Section 3.3.3, CFLC is the limiting criteria when the flow velocity is low, but for high flow velocities, the CFLV criteria is activated, following Equation 3.8. The deviating result for 20 m/s with CFLC/CFLV 10/1 will be used as an example. The speed of sound in an ideal gas is (McCabe et al., 2005, p. 137):

$$a = \sqrt{\frac{\gamma p}{\rho}} \tag{4.1}$$

where γ is the isentropic expansion ratio. The speed of sound is ~ 340 m/s in the reactants, the expansion ratio from cold reactants to hot products is ~ 7.6, and the speed of sound in products can therefore be estimated to:

$$a_P = \sqrt{\frac{\gamma p}{\rho_R \frac{\rho_P}{\rho_R}}} = a_R \sqrt{\frac{1}{\rho_P/\rho_R}} = 340\sqrt{\frac{1}{1/7.6}} \approx 940 \text{ m/s} \tag{4.2}$$

The highest flow velocities are in the reactants that are being pushed forward by the expansion. Equation 3.1 yields:

$$U = S_\mathrm{f} - S = S \cdot E - S = S(E-1) \tag{4.3}$$

For a burning velocity of 20 m/s, this results in a flow velocity ahead of the flame of:

$$U = 20(7.6 - 1) \approx 130 \text{ m/s} \tag{4.4}$$

Inserting the approximate values for a and U into Equation 3.8 yields:

$$\Delta t = \min\left(\frac{1 \cdot 0.1}{130}, \frac{10 \cdot 0.1}{940}\right) = \min\left(7.7 \cdot 10^{-4}, 1.1 \cdot 10^{-3}\right) \tag{4.5}$$

The time step size will therefore be based on the flow velocity in the case of $S = 20$ m/s, and CFL= 10/1. With $S_f = 20 \cdot 7.6 \approx 150$ m/s, the flame should move the length l in each time step:

$$l \approx 150 \text{ m/s} \cdot 7.7 \cdot 10^{-4} \text{ s} = 0.12\text{m} \tag{4.6}$$

As $l > \Delta x$, SIF can not handle these conditions. To ensure that the time step size is long enough at high flame speeds, it would therefore be necessary to include a stricter time step criteria when SIF is used.

4.4 SIF open end ignition

The simple interface flame model provided very accurate results for the lowest burning velocities tested with open end ignition. However, as the burning velocity was increased, the flame speed started to periodically accelerate, and then be stationary. The reason for this is explained in Section 3.7.1. The reactants between the flame and the closed end wall is compressed, and flow of reactants towards the wall is initiated. After a short time, the flow is reversed, and thus causing a flow towards the flame at a velocity close to the flame speed. The approaching reactant flow is effectively feeding the flame, keeping it stationary. In the constantly oscillating system, it is hard to measure the flame speed, and it is therefore advised to make the channel longer. By keeping the closed end far away from the open end, the reactant flow will keep flowing away from the flame. Though not ideal, this makes it easier to measure the flow velocity, and subtracting it from the flame speed, to get the flame speed relative to the reactants. Results from simulations with the long channel is briefly described in Section 3.7.1.

4.5 Fourier number

The Fourier number (see Section 3.2) was calculated for the simulations with the β model. For most simulations, some value of the Fourier number defined the limit between converged and non converged flame speeds. The upper limit for the Fourier numbers are summarised in Table 4.1. With the exception of the open end ignition simulation where the correction function is turned off, 0.003 is a sufficiently low Fourier number to cause convergence. A time step criteria can be based on the Fourier number by rearranging Equation 3.2 and 3.3:

$$\Delta t = \frac{Fo}{\mathcal{D}}(\Delta x)^2 = \frac{Fo}{SC\Delta x}(\Delta x)^2 = \frac{Fo\Delta x}{SC} \tag{4.7}$$

Table 4.1: Upper Fourier number limit for convergence

Case	Fourier number
β model closed end, correction enabled	0.005
β model closed end, correction disabled	0.003
β model closed end, van Leer	0.003
β model open end, correction enabled	0.006
β model open end, correction disabled	NA
β model open end, correction enabled, double flame	0.006
β model open end, correction disabled, double flame	0.006

Chapter 5

Conclusion and recommendations

The β flame model in FLACS results in a lower flame speed than what is expected for closed end ignition in a 1D-channel. For small time steps, the flame speed converges towards a flame speed $\sim$ 27 % lower than the correct value. For open end ignition, the β flame model results in flame speeds close to the correct value. Improved results can be obtained by turning off an inbuilt function in FLACS that corrects for long time steps. Flame speed measurement for open end ignition is also difficult because the reactants ahead of the flame will flow as a result of pressure gradients in the channel. This can be taken into account by extending the channel, and subtracting the flow velocity of the reactants.

The SIF-model in FLACS performs well for both closed end and open end ignition. A stricter time step criteria may however be included to avoid problems at high velocities and time steps.

A Fourier number may be introduced in FLACS as a time step criteria for converged flame speeds. Values below 0.003 gives convergence for the simulations conducted.

As the flame speed encountered with the β model for closed end ignition is too low, it may be necessary to adjust the model to account for the reduced numerical diffusion in the new numerical scheme introduced in FLACS.

Bibliography

Arntzen, B. J. (1998). *Modelling of turbulence and combustion for simulation of gas explosions in complex geometries*. PhD thesis, Norwegian University of Science and Technology, Trondheim.

Borghi, R. (1985). On the structure and morphology of turbulent premixed flames. In C. Casci, editor, *Recent advances in the Aerospace Sciences*, pages 117–138. Plenum Publishing Corporation.

Cullen, H. (1990). *The public inquiry into the Piper Alpha disaster (Report to the Parliament by the Secretary of State for Energy by Command of Her Majesty)*. London: HMSO.

Czujko, J., editor (2001). *Design of offshore facilities to resist gas explosion hazard: engineering handbook*. CorrOcean ASA, Sandvika.

Eckhoff, R. K. (2005). *Explosion hazards in the process industries*. Gulf Publishing Company, Houston.

Ertesvåg, I. S. (2000). *Turbulent strøyming og forbrenning: frå turbulensteori til ingeniørverkty*. Tapir akademisk forlag, Trondheim.

Favre, A. (1965). Équations des gaz turbulents compressibles. *J. Mécanique*, 4:361–421.

Favre, A. (1969). Statistical equations of turbulent gases: contributions in honor of the sixtieth birthday of L. I. Sedov, 14th november 1967. In Block, J. E., editor, *Problems of hydrodynamics and continuum mechanics*, pages 231–266. Society for Industrial and Applied Mathematics, Philadelphia.

GexCon AS (2013). *FLACS v10.1 User's Manual*.

Holman, J. P. (2010). *Heat Transfer*. McGraw-Hill, New York, tenth edition.

IEA (2013). *Key World Energy Statistics 2013*. OECD/IEA.

Launder, B. E. and Spalding, D. B. (1974). The numerical computation of turbulent flows. *Computer methods in applied mechanics and engineering*, 3:269–289.

Magnussen, B. F. and Hjertager, B. H. (1977). On mathematical modeling of turbulent combustion with special emphasis on soot formation and combustion. In *Symposium (International) on Combustion*, volume 16, pages 719–729. Elsevier.

McCabe, W. L., Smith, J. C., and Harriott, P. (2005). *Unit Operations of Chemical Engineering*. McGraw-Hill, New York.

Model Evaluation Group Gas Explosions (MEGGE) (1996). *Gas explosion model evaluation protocole Version 1*. Model Evaluation Group Gas Explosions (MEGGE).

Narasimhamurthy, V. D. (2009). Turbulent wake behind a normal flat plate. Digital Image. https://sites.google.com/site/vageshdn/. Last accessed on May 14, 2014.

Park, D. J. and Lee, Y. S. (2009). A comparison on predictive models of gas explosions. *Korean Journal of Chemical Engineering*, 26(2):313–323.

Peters, N. (2000). *Turbulent combustion*. Cambridge university press, Cambridge.

Peters, N. (2013). Turbulent combustion. Lectures given at the Combustion Institute Summer School, Lund.

Poinsot, T. and Veynante, D. (2005). *Theoretical and numerical combustion*. RT Edwards, Inc., Philadelphia.

Reynolds, O. (1895). On the dynamical theory of incompressible viscous fluids and the determination of the criterion. *Philosophical Transactions of the Royal Society of London. A*, pages 123–164.

Skjold, T., van Wingerden, K., Storvik, I. E., Pesch, L., Melheim, J. A., Ichard, M., Narasimhamurthy, V. D., Middha, P., Pedersen, H. H., Bernard, L., Hansen, O. R., Lilleberg, B., and Khalil, M. (2013). Final report 'JIP FLACS 2011 and beyond'. Technical Report GexCon-13-F46240-C-1, GexCon AS, Bergen. Confidential.

Spalding, D. (1971). Mixing and chemical reaction in steady confined turbulent flames. *Symposium (International) on Combustion*, 13(1):649 – 657. The Combustion Institute, Pittsburgh.

Turns, S. R. (2012). *An introduction to combustion: Concepts and applications*. McGraw-Hill, New York.

Warnatz, J., Maas, U., and Dibble, R. W. (2006). *Combustion: physical and chemical fundamentals, modeling and simulation, experiments, pollutant formation*. Springer, Berlin.

Wilcox, D. C. (1994). *Turbulence Modeling for CFD*. DCW Industries, Inc., California.